Dyes and Pigments 252 (2026) 113772

Contents lists available at ScienceDirect

Dyes and Pigments

journal homepage: www.elsevier.com/locate/dyepig

# Azobenzene-triindole hybrid chromophores as light-responsive organic semiconductors: Synthesis, photoisomerization and semiconducting properties

Clara Fabregat [a,b], Jaume Garcia-Amorós [a,b], Dmytro Volyniuk [c], Juozas V. Grazulevicius [c], Dolores Velasco [a,b,*]

[a] Grup de Materials Orgànics, Departament de Química Inorgànica i Orgànica, Secció de Química Orgànica, Universitat de Barcelona, Martí i Franquès 1, E-08028, Barcelona, Spain
[b] Institut de Nanociència i Nanotecnologia (IN$^2$UB), E-08028, Barcelona, Spain
[c] Department of Polymer Chemistry and Technology, Kaunas University of Technology, Radvilenu Plentas 19, LT-50254, Kaunas, Lithuania

ARTICLE INFO

*Keywords:*
Azobenzene
Triindole
Photoresponsive
Organic semiconductors
Light-addressable materials

ABSTRACT

Azobenzene (AB) chromophores are among the most widely utilized molecular photoswitches; however, their integration into organic semiconductor (OSC) frameworks to enable orthogonal light-driven control of the electronic properties while maintaining efficient charge transport remains a significant challenge. Herein, we report the design and synthesis of a series of novel photoactive OSCs hybrids in which AB units have been integrated into the OSC backbone of 10,15-dihydro-5*H*-diindolo[3,2-*a*:3′,2′-*c*]carbazole, namely triindole. Structural variations involving the number of AB units, their functionalization site and the incorporation of alkoxy spacers have been employed to systematically evaluate and monitor their photophysical and electronic properties. As a result, all the derivatives presented photoactivity, exhibiting a bistable behavior with efficient and reversible photoisomerization in both solution and solid phase under UV or visible light irradiation. Additionally, these materials displayed excellent thermal robustness ($T_d$ > 350 °C) and appropriate HOMO-LUMO energy levels for air stable p-type OSCs. Time-of-flight measurements further confirmed efficient hole transport, with mobilities reaching up to 1.5 × $10^{-4}$ $cm^2$ $V^{-1}$ $s^{-1}$ under an applied electric field of 6 × $10^5$ V $cm^{-1}$. Hence, the combination of outstanding photoresponsiveness and favorable semiconducting properties establishes these AB-triindole hybrids as promising building blocks for future photoactive and light-addressable electronic devices.

## 1. Introduction

Light-responsive molecular systems, commonly referred to as photoswitches, constitute a powerful platform for the remote and reversible modulation of material properties through an optical stimulus. That is, the photoinduced state events trigger well-defined structural rearrangements at the molecular level, which can propagate to measurable changes in the macroscopic properties. In the context of organic electronics and transistor technologies, this light-driven molecular reconfiguration enables the modulation of the electrical signal through the combined action of electrical stress and optical input, thereby opening avenues for applications ranging from photodetectors [1,2] to photo-assisted information storage [3–5]. Among the wide variety of molecular photoswitches, azobenzenes (ABs) are particularly prominent due to their robust and reversible isomerization between the *trans* and *cis* states, which grants access to two distinct molecular states with differentiated physicochemical properties [6–8]. In addition to light-induced switching, the *cis* isomer also undergoes thermal *cis*-to-*trans* relaxation in the dark, a process that is highly sensitive to chemical functionalization [8–11]. For example, azoderivatives bearing a weak push-pull configuration normally exhibit half-lives in the hour scale in solution [12,13].

Despite this attractive feature, AB compounds generally display minimal charge-transport characteristics [14]. Consequently, the integration of these photochromic entities into established organic semiconductor (OSC) frameworks represents an attractive strategy to impart

* Corresponding author. Grup de Materials Orgànics, Departament de Química Inorgànica i Orgànica, Secció de Química Orgànica, Universitat de Barcelona, Martí i Franquès 1, E-08028, Barcelona, Spain.
*E-mail address:* dvelasco@ub.edu (D. Velasco).

https://doi.org/10.1016/j.dyepig.2026.113772
Received 24 March 2026; Received in revised form 9 April 2026; Accepted 9 April 2026
Available online 9 April 2026

light-addressable functionality while retaining charge-transport capability. However, achieving an optimal balance between these two properties remains a non-trivial challenge, and only a few examples of single-component photoresponsive OSCs can be found in the literature [15,16]. Compared to strategies based on integrating isolated ABs in device interlayers, the covalent incorporation of the AB unit into the OSC enables the modulation of the intrinsic transport properties through light-induced changes in molecular packing and film morphology, while simultaneously simplifying the device architecture. In this regard, the compound 10,15-dihydro-5*H*-diindolo[3,2-*a*:3′,2′-*c*]carbazole, commonl y known as triindole, constitutes a notable p-type OSC, which possesses excellent hole-transport characteristics and air stability [17,18]. Additionally, its molecular architecture offers multiple functionalization sites, including the nitrogen heteroatoms and the peripheral 3,8,13 and 2,7,12 positions.

With this in mind, we engaged in the design of an asset of novel photosensitive materials by grafting the *para*-alkoxy-substituted AB moieties as the photochromic component and the triindole scaffold as the OSC unit (Fig. 1). Two principal substitution patterns were explored: derivatization at the nitrogen positions (*N*-AB-triindoles, **1**–**3**) or at the 3,8,13 positions of the triindole core (*C*-AB-triindoles, **4**). The photoresponsive behavior of these systems was examined using complementary spectroscopic techniques to assess light-induced *trans-cis* isomerization, reversibility and *cis* stability in solution and in the solid state. For the semiconducting properties, frontier energy levels were evaluated and time-of-flight (TOF) measurements were conducted to examine charge-carrier transport. Together, this multifaceted approach establishes a framework for assessing the suitability of the AB-triindole hybrids reported herein as photoresponsive OSCs and lays the groundwork for future studies toward light-addressable electronic materials.

## 2. Experimental section

### 2.1. Instrumentation and methods

Nuclear magnetic resonance (NMR) spectra were acquired in a Bruker 400 MHz Advance III instrument for $^{1}$H NMR (400 MHz) and $^{13}$C NMR spectra (101 MHz). The resulting NMR spectra were processed with MestReNova software (version 14.0.0-23239) and referenced using the solvent signal.

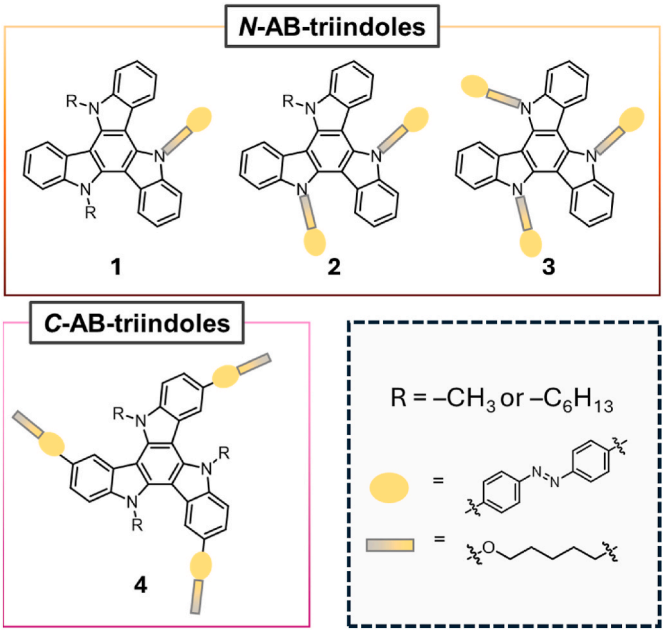


**Fig. 1.** Schematic representation of *N*-(**1**–**3**) and *C*-AB-triindole (**4**) derivates studied within this work.

IR spectra (Attenuated Total Reflectance, ATR) were recorded using a Nicolet 6700 FT-IR Thermo Scientific spectrometer and the more representative frequencies ($\nu$) are reported in cm$^{-1}$.

The melting points ($M_p$) were determined with a Cole-Parmer MP-800D Series apparatus using a heating rate of 3 °C min$^{-1}$.

High-resolution mass spectrometry (HRMS) was performed using an Agilent Technologies LC/MSD-TOF system with an electrospray ionization (ESI-MS) source. Matrix-assisted laser desorption/ionization time-of-flight mass spectra (MALDI-TOF-MS) analysis was conducted on an Applied Biosystems MDS SCIEX 4800 instrument in Reflector mode.

Absorption spectra of solutions were prepared in toluene (10 μM) and recorded in a Varian Cary UV-Vis-NIR 500E spectrophotometer. All solution experiments were measured using 1 cm optical path quartz cells (Hellma). For solid-state measurements, a solution containing the chromophore (1 mg/mL) was dropcasted onto a quartz substrate and left it slowly evaporate to promote film formation. Photoisomerization was performed placing a light source at approximately 3 cm from the quartz cuvette. *Trans*-to-*cis* AB photoisomerization was conducted using either a Thorlabs Collimated laser diode module CPS405 (deep blue light, 405 nm, 4.5 mW) or a Hamamatsu LED L14310-110 (UV light, 365 nm, 35 mW) controlled by a UV-LED spot light source LIGHTNINGCURE LC-L1V5. For the *cis*-to-*trans* back-photoisomerization it was used a Thorlabs Collimated laser diode module CPS450 (sky blue light, 450 nm, 4.5 mW) or CPS520 (green light, 520 nm, 4.5 mW). In contrast, *cis*-to-*trans* thermal relaxation was kinetically followed by UV-Vis and measured in the dark and the temperature was controlled by a heating immersion circulator Julabo F12-MC.

Cyclic voltammograms were obtained using a microcomputer-controlled potentiostat/galvanostat Autolab with PGSTAT30 equipment and GPES software (version 4.9) in a cylindrical three-electrode cell. The reference was an Ag/Ag$^{+}$ electrode ($10^{-3}$ M $AgNO_3$ in acetonitrile), the working electrode was a glassy-carbon electrode, and the counter electrode was a platinum wire. The compounds were dissolved in distilled $CH_2Cl_2$ ($10^{-3}$ M) and tetrabutylammonium hexafluorophosphate (TBAP, 0.1 M) was employed as the supporting electrolyte. All voltammograms were collected under quiescent conditions and under argon atmosphere at a scan rate of 100 mV s$^{-1}$. The resulting potentials were referenced to the Fc$^{+}$/Fc redox couple. The resultant ionization potentials ($IP_{CV}$) were estimated from the onset of the first oxidation peak ($E^{ox}_{onset}$) as $IP = E^{ox}_{onset} + 5.39$, where 5.39 eV corresponds to the formal potential in the Fermi scale of the Fc$^{+}$/Fc couple. The electron affinities (EA) were estimated as $EA = IP_{CV} - (E^{opt}_{gap})$. The optical energy bandgap ($E^{opt}_{gap}$) were estimated from the onset wavelength of the absorption spectra.

Ionization potential of solid samples ($IP_{PE}$) were obtained by electron photoemission spectrometry (PES) in air using a setup composed of ASBN-D130-CM deep UV deuterium light source, CM110 1/8 m monochromator and 6517B Keithley electrometer. Pristine samples were vacuum-deposited onto fluorine-doped tin oxide (FTO) coated glass slides as substrate. bisphenol Z-polycarbonate (PC-Z) doped films were formed by formulating films with the chromophore (1:1 w/w; 1 mg/mL in toluene) and dropcasted in FTO coated glass slides. The PES spectra were recorded by exciting the samples from low energy to high energy with a step of 1 nm and recording an electron photoemission current at different excitation energies.

The samples for time-of-flight (TOF) measurements were prepared by vacuum thermal evaporation onto 100-nm-thick indium-tin oxide (ITO) coated glass substrates under a base pressure below $10^{-6}$ mbar. Then, the aluminum electrodes (1 μm) were also deposited by vacuum evaporation using a shadow mask. Film thicknesses were determined with a Profilm3D profilometer from cross-sectional cuts. Charge carriers were generated using a pulsed Nd:YAG laser EKSPLA NL300 ($\lambda_{Ex} = 355$ nm, pulse duration 3–6 ns). A voltage at the sample surface was adjusted using a Keithley 6517B electrometer and the photocurrent transients

were recorded on a Tektronix TDS 3032C oscilloscope. The transit times ($t_t$) were extracted from the kink on the log-log plot of the transient photocurrent. The drift mobility ($\mu$) was calculated by the formula $\mu = d^2/U\,t_t$, where d is the layer thickness, and $U$ is the surface potential at the moment of illumination. Zero-field mobilities ($\mu_0$) and the field dependence parameter (α) were calculated by the equation: $\mu = \mu_0\, e^{\alpha E1/2}$, where $E$ is the applied electric field.

### 2.2. Synthetic procedure

#### 2.2.1. Synthesis of 1-(4-((6-bromohexyl)oxy)phenyl)-2-phenyldiazene (6)

4-Hydroxyazobenzene (4.00 g, 20.2 mmol) and $PPh_3$ (5.82 g, 22.2 mmol) were dissolved in dry THF (100 mL) under nitrogen atmosphere. Then, DIAD (4,36 mL, 22.2 mmol) and 6-bromo-1-hexanol (2.90 mL, 22.2 mmol) were added and left stirring for 2 days at room temperature. The mixture was removed under reduced pressure and the crude product was purified by flash column chromatography using a mixture of hexane and $CH_2Cl_2$ (4:1 v/v) as the eluent to give **6** as an orange solid in 67% yield (4.86 g, 13.5 mmol).

$R_f$: 0.46 (Hexane:$CH_2Cl_2$ 4:1 v/v). $M_p$ 73 °C. IR (ATR): 2939, 2859, 1601, 1578, 1498, 1463, 1238, 1142, 1103, 995, 837, 764, 684 $cm^{-1}$. $^1H$ NMR (400 MHz, $CDCl_3$) $\delta$ (ppm): 7.94 – 7.89 (m, 2H), 7.89 – 7.84 (m, 2H), 7.53 – 7.47 (m, 2H), 7.46 – 7.40 (m, 1H), 7.04 – 6.96 (m, 2H), 4.05 (t, $J = 6.5$ Hz, 2H), 3.46 – 3.37 (m, 2H), 1.96 – 1.81 (m, 4H), 1.57 – 1.50 (m, 4H).

**General procedure reaction iii. and iv. (1–3)**: triindole **7** (150 mg, 0.43 mmol, 1 eq.) was dissolved in anhydrous DMF (10 mL) under nitrogen atmosphere and then NaH (60% dispersion in mineral oil) was added and the mixture was left stirring for 30 min at room temperature. Afterwards, **6** was added and the reaction was heated to 100 °C overnight. Then, the reaction was cooled down to room temperature and for the subsequent reaction iv, additional NaH (3 eq.) and MeI or 1-bromohexane (3 eq.) were added. The resulting reaction mixture was stirred for 5 h at room temperature. The mixture was diluted with water (ca. 150 mL) and extracted with EtOAc. The combined organic extract was dried over anhydrous $MgSO_4$, filtered and the solvent was removed under reduced pressure. The crude product was purified by flash column chromatography to obtain the final *N*-AB-triindoles derivatives **1**–**3**.

#### 2.2.2. Synthesis of 5,10-dimethyl-15-(6-(4-(phenyldiazenyl)phenoxy) hexyl)-10,15-dihydro-5H-diindolo[3,2-a:3′,2′-c]carbazole (1a)

As described in **General Procedure**, **7** (150 mg, 0.43 mmol) and NaH (53 mg, 1.33 mmol, 60% dispersion in mineral oil) were used. **6** (171 mg, 0.47 mmol) was added and the reaction was heated to 100 °C overnight. Additional NaH (52 mg, 1.30 mmol, 60% dispersion in mineral oil) and MeI (81 μL, 1.30 mmol) were added for reaction iv. The crude product was purified by flash column chromatography using a mixture of hexane and $CH_2Cl_2$ (4:1 v/v) as eluent to give compound **1a** as an orange-yellowish solid in 37% yield (106 mg, 0.16 mmol).

$R_f$: 0.60 (Hexane:$CH_2Cl_2$ 1:2 v/v). $M_p$ 150 °C. IR (ATR): 2922, 2856, 1577, 1560, 1467, 1245, 1140, 829, 743 $cm^{-1}$. $^1H$ NMR (400 MHz, $CDCl_3$) $\delta$ (ppm): 8.52 – 8.40 (m, 2H), 8.34 – 8.26 (m, 1H), 7.94 – 7.83 (m, 4H), 7.71 – 7.57 (m, 3H), 7.54 – 7.41 (m, 6H), 7.39 – 7.32 (m, 3H), 6.96 – 6.87 (m, 2H), 5.04 – 4.95 (m, 2H), 4.48 – 4.41 (m, 6H), 3.88 (t, $J = 6.5$ Hz, 2H), 2.14 – 2.00 (m, 2H), 1.76 – 1.65 (m, 2H), 1.52 – 1.32 (m, 4H). $^{13}C$ NMR (101 MHz, $CDCl_3$) $\delta$ (ppm): 161.5, 152.8, 146.8, 142.4, 142.1, 140.7, 139.3, 139.2, 138.6, 130.3, 129.0 (2C), 124.7 (2C), 123.2, 123.0 (2C), 122.8, 122.7 (2C), 122.5 (2C), 121.9, 121.7, 121.4, 119.9 (2C), 119.6, 114.6 (2C), 110.2, 109.8 (2C), 102.9, 102.7 (2C), 67.9, 46.5, 36.2 (2C), 36.1, 29.9, 28.9, 26.3, 25.7. HRMS (ESI+) *m/z*: calcd. for $C_{44}H_{40}N_5O$ $(M + H)^+$, 654,3227; found 654.3222.

#### 2.2.3. Synthesis of 5,10-dihexyl-15-(6-(4-(phenyldiazenyl)phenoxy) hexyl)-10,15-dihydro-5H-diindolo[3,2-a:3′,2′-c]carbazole (1b)

As described in **General Procedure**, **7** (150 mg, 0.43 mmol) and NaH (53 mg, 1.33 mmol, 60% dispersion in mineral oil) were used. **6** (171 mg, 0.47 mmol) was added and the reaction was heated to 100 °C overnight. Additional NaH (52 mg, 1.30 mmol, 60% dispersion in mineral oil) and MeI (81 μL, 1.30 mmol) were added for reaction iv. The crude product was purified by flash column chromatography using a mixture of hexane and $CH_2Cl_2$ (4:1 v/v) as eluent to give compound **1b** as an orange-yellowish solid in 27% yield (92 mg, 0.12 mmol).

$R_f$: 0.50 (Hexane:$CH_2Cl_2$ 1:2 v/v). $M_p$ 80 °C. IR (ATR): 2920, 2855, 1560, 1472, 1407, 1252, 1141, 833, 792, 768, 744 $cm^{-1}$. $^1H$ NMR (400 MHz, $CDCl_3$) $\delta$ (ppm): 8.32 – 8.25 (m, 3H), 7.90 – 7.83 (m, 4H), 7.67 – 7.60 (m, 3H), 7.54 – 7.39 (m, 6H), 7.38 – 7.29 (m, 3H), 6.92 – 6.86 (m, 2H), 4.98 (t, $J = 7.7$ Hz, 2H), 4.92 (t, $J = 8.0$ Hz, 4H), 3.84 (t, $J = 6.4$ Hz, 2H), 2.05 – 1.90 (m, 6H), 1.67 – 1.61 (m, 2H), 1.43 – 1.37 (m, 2H), 1.37 – 1.16 (m, 14H), 0.80 (t, $J = 7.0$ Hz, 6H). $^{13}C$ NMR (101 MHz, $CDCl_3$) $\delta$ (ppm): 161.6, 152.8, 146.8, 141.0 (3C), 138.9 (3C), 130.3, 129.0 (2C), 124.7 (2C), 123.4 (3C), 122.7 (3C), 122.5 (2C), 121.5 (3C), 119.7 (3C), 114.6 (2C), 110.7, 110.5 (2C), 103.2 (3C), 67.9, 47.0 (2C), 46.8, 31.4 (2C), 29.8 (2C), 29.4, 28.8, 26.4 (2C), 26.2, 25.6, 22.5 (2C), 13.9 (2C). HRMS (ESI+) *m/z*: calcd. for $C_{54}H_{60}N_5O$ $(M + H)^+$, 794.4792; found 794.4794.

#### 2.2.4. Synthesis of 5-methyl-10,15-bis(6-(4-(phenyldiazenyl)phenoxy) hexyl)-10,15-dihydro-5H-diindolo[3,2-a:3′,2′-c]carbazole (2a)

As described in **General Procedure**, **7** (150 mg, 0.43 mmol) and NaH (70 mg, 1.75 mmol, 60% dispersion in mineral oil) were used. **6** (327 mg, 0.90 mmol) was added and the reaction was heated to 100 °C overnight. Additional NaH (52 mg, 1.30 mmol, 60% dispersion in mineral oil) and 1-bromohexane (1.82 mL, 1.30 mmol) were added for reaction iv. The crude product was purified by flash column chromatography using a mixture of hexane and $CH_2Cl_2$ (4:1 v/v) as eluent to give compound **2a** as an orange-yellowish solid in 27% yield (109 mg, 0.12 mmol).

$R_f$: 0.65 (Hexane:$CH_2Cl_2$ 1:2 v/v). $M_p$ 52 °C. IR (ATR): 2920, 2855, 1579, 1467, 1329, 1243, 1139, 1098, 833, 766, 744 $cm^{-1}$. $^1H$ NMR (400 MHz, $CDCl_3$) $\delta$ (ppm): 8.44 (d, $J = 8.0$ Hz, 1H), 8.38 – 8.25 (m, 2H), 7.92 – 7.81 (m, 8H), 7.68 – 7.59 (m, 3H), 7.54 – 7.41 (m, 9H), 7.39 – 7.30 (m, 3H), 6.96 – 6.82 (m, 4H), 5.06 – 4.90 (m, 4H), 4.42 (s, 3H), 3.90 – 3.81 (m, 4H), 2.09 – 1.95 (m, 4H), 1.75 – 1.62 (m, 4H), 1.48 – 1.24 (m, 8H). $^{13}C$ NMR (101 MHz, $CDCl_3$) $\delta$ (ppm): 161.5 (2C), 152.8 (2C), 146.8 (2C), 142.4, 141.0, 140.8, 139.4, 138.8, 138.7, 130.3 (2C), 129.0 (4C), 124.7 (4C), 123.5, 123.3, 123.1, 123.0, 122.8 (2C), 122.5 (4C), 121.9, 121.5, 121.4, 119.9, 119.8, 119.7, 114.6 (4C), 110.5 (2C), 109.9, 103.2, 103.1, 103.0, 67.9 (2C), 46.7 (2C), 36.2, 29.7 (2C), 28.9 (2C), 26.3 (2C), 25.6 (2C). HRMS (ESI+) *m/z*: calcd. for $C_{61}H_{58}N_7O_2$ $(M + H)^+$, 920.4647; found 920.4631.

#### 2.2.5. Synthesis of 5-hexyl-10,15-bis(6-(4-(phenyldiazenyl)phenoxy) hexyl)-10,15-dihydro-5H-diindolo[3,2-a:3′,2′-c]carbazole (2b)

As described in **General Procedure**, **7** (150 mg, 0.43 mmol) and NaH (70 mg, 1.75 mmol, 60% dispersion in mineral oil) were used. **6** (327 mg, 0.90 mmol) was added and the reaction was heated to 100 °C overnight. Additional NaH (52 mg, 1.30 mmol, 60% dispersion in mineral oil) and 1-bromohexane (1.82 mL, 1.30 mmol) were added for reaction iv. The crude product was purified by flash column chromatography using a mixture of hexane and $CH_2Cl_2$ (4:1 v/v) as eluent to give compound **2b** as an orange-yellowish solid in 35% yield (149 mg, 0.15 mmol).

$R_f$: 0.52 (Hexane:$CH_2Cl_2$ 2:1 v/v). $M_p$ 56 °C. IR (ATR): 2920, 2853, 1579, 1467, 1243, 1137, 1103, 833, 764, 746 $cm^{-1}$. $^1H$ NMR (400 MHz, $CDCl_3$) $\delta$ (ppm): 8.31 – 8.24 (m, 3H), 7.90 – 7.82 (m, 8H), 7.68 – 7.60 (m, 3H), 7.53 – 7.40 (m, 9H), 7.37 – 7.31 (m, 3H), 6.91 – 6.85 (m, 4H), 5.02 – 4.95 (m, 4H), 4.91 (t, $J = 8.2$ Hz, 2H), 3.83 (t, $J = 6.5$ Hz, 4H), 2.07 – 1.89 (m, 6H), 1.67 – 1.57 (m, 4H), 1.44 – 1.17 (m, 14H), 0.80 (t, $J = 7.0$ Hz, 3H). $^{13}C$ NMR (101 MHz, $CDCl_3$) $\delta$ (ppm): 161.5 (2C), 152.8 (2C), 146.8 (2C), 141.0 (3C), 138.9 (3C), 130.3 (2C), 129.0 (4C), 124.7 (4C), 123.6 (2C), 123.3, 122.8 (3C), 122.5 (4C), 121.5 (3C), 119.7 (3C), 114.6 (4C), 110.7 (2C), 110.5, 103.3 (3C), 67.92 (2C), 47.0 (3C), 31.4, 29.8,

29.4 (2C), 28.9 (2C), 26.4, 26.2 (2C) 25.6 (2C), 22.5, 13.9. HRMS (ESI+) *m/z*: calcd. for $C_{66}H_{68}N_7O_2$ $(M + H)^+$, 990.5429; found 990.5409.

### 2.2.6. Synthesis of 5,10,15-tris(6-(4-(phenyldiazenyl)phenoxy)hexyl)-10,15-dihydro-5H-diindolo[3,2-a:3′,2′-c]carbazole (3)

As described in **General Procedure**, **7** (150 mg, 0.43 mmol) and NaH (105 mg, 2.63 mmol, 60% dispersion in mineral oil) were used. **6** (950 mg, 2.63 mmol) was added and the reaction was heated to 100 °C overnight. The crude product was purified by flash column chromatography using a mixture of hexane and $CH_2Cl_2$ (4:1 v/v) as eluent to give compound **3** as an orange-yellowish solid in 71% yield (392 mg, 0.33 mmol).

$R_f$: 0.30 (Hexane:$CH_2Cl_2$ 1:2 v/v). $M_p$ 52 °C. IR (ATR): 2930, 2851, 1597, 1579, 1498, 1467, 1246, 1139, 835, 766, 747, 727, 688 $cm^{-1}$. $^1H$ NMR (400 MHz, $CDCl_3$) $\delta$ 8.35 – 8.21 (m, 3H), 7.90 – 7.82 (m, 12H), 7.68 – 7.62 (m, 3H), 7.54 – 7.40 (m, 12H), 7.36 – 7.32 (m, 3H), 6.90 – 6.80 (m, 6H), 4.97 (t, $J = 7.8$ Hz, 6H), 3.82 (t, $J = 6.5$ Hz, 6H), 2.05 – 1.90 (m, 6H), 1.69 – 1.56 (m, 6H), 1.45 – 1.33 (m, 6H), 1.33 – 1.19 (m, 6H). $^{13}C$ NMR (101 MHz, $CDCl_3$) 161.5, 152.8, 146.8, 141.0, 138.9, 130.3, 129.0 (2C), 124.7 (2C), 123.5, 122.9, 122.5 (2C), 121.6, 119.8, 114.6 (2C), 110.7, 103.3, 67.9, 46.8, 29.5, 28.9, 26.2, 25.6. HRMS (ESI+) *m/z*: calcd. for $C_{78}H_{76}N_9O_3$ $(M + H)^+$, 1186.5993; found 1186.5994.

### 2.2.7. Synthesis of 4′-hydroxy-4-bromoazobenzene (8)

4-bromoaniline (10.0 g, 58.1 mmol) was dissolved in a mixture of cold water and 37% aq. HCl (120 mL, 2:1 v/v) and it was cooled to 0 °C in an ice bath. Then, a solution of $NaNO_2$ (3.34 g, 48.4 mmol) in cold water (20 mL) was added slowly to the mixture and stirred for 2 h. Afterwards, a solution of phenol (5.17 g, 54.9 mmol) and NaOH (14.1 g, 353 mmol) in cold water (75 mL) is added dropwise and stirred for 1 h. The solution was acidified with HCl (1 M) to pH = 4–5 and the organic phase was extracted with $CH_2Cl_2$, dried over anhydrous $MgSO_4$ and the solvent was removed under reduced pressure. The crude product was purified by flash column chromatography with a mixture of hexane and EtOAc (8:1 v/v) as the eluent to obtain compound **8** as an orange solid in 70% yield (11.3 g, 40.8 mmol).

$R_f$: 0.48 (Hexane:EtOAc 5:1 v/v). $M_p$ 158 °C. IR (ATR): 3112, 1569, 1472, 1396, 1219, 1101, 1062, 1005, 833, 723 $cm^{-1}$. $^1H$ NMR (400 MHz, $CDCl_3$) $\delta$ (ppm): 7.91 – 7.84 (m, 2H), 7.79 – 7.72 (m, 2H), 7.67 – 7.59 (m, 2H), 6.98 – 6.92 (m, 2H), 5.18 (s, 1H).

### 2.2.8. Synthesis of 4′-hexyloxy-4-bromoazobenzene (9)

**8** (2.00 g, 7.22 mmol) was dissolved in anhydrous DMF (10 mL) under nitrogen atmosphere and then NaH (432 mg, 10.8 mmol, 60% dispersion in mineral oil) was added and left stirring for 30 min at room temperature. Then 1-bromohexane (2.00 mL, 14.2 mmol) was added and the reaction was stirred overnight. The mixture was diluted with water (ca. 150 mL) and the precipitate was filtered, washed with water and dried. The crude product was purified by flash column chromatography using a mixture of hexane and $CH_2Cl_2$ (5:1 v/v) as the eluent to obtain **9** as an orange solid in 95% yield (2.49 g, 6.89 mmol).

$R_f$: 0.31 (Hexane:$CH_2Cl_2$ 5:1 v/v). $M_p$ 93 °C. IR (ATR): 2943, 2920, 2851, 1580, 1498, 1463, 1415, 1388, 1254, 1109, 1064, 1025, 833, 800, 723 $cm^{-1}$. $^1H$ NMR (400 MHz, $CDCl_3$) $\delta$ (ppm): 7.93 – 7.86 (m, 2H), 7.79 – 7.72 (m, 2H), 7.65 – 7.59 (m, 2H), 7.03 – 6.97 (m, 2H), 4.04 (t, $J = 6.6$ Hz, 2H), 1.87 – 1.78 (m, 2H), 1.53 – 1.44 (m, 2H), 1.41 – 1.31 (m, 4H), 0.92 (t, $J = 5.1$ Hz, 3H).

### 2.2.9. Synthesis of 4′-hexyloxy-4-azobenzeneboronic acid pinacol ester (10)

**9** (1.00 g, 2.77 mmol), $B_2Pin_2$ (0.84 g, 3.30 mmol) and NaOAc (0.50 g, 6.10 mmol) were dissolved in toluene (10 mL) under nitrogen atmosphere. Then, $Pd(PPh_3)_2Cl_2$ (0.078 g, 0.111 mmol) was added and stirred for 24 h at 90 °C. The solution was extracted with EtOAc, dried over anhydrous $Na_2SO_4$ and the solvent was removed under reduced pressure. The crude product was purified by flash column chromatography with a mixture of hexane and EtOAc (50:1 v/v) as the eluent to obtain compound **10** as an orange solid in 67% yield (0.76 g, 1.86 mmol).

$R_f$: 0.45 (Hexane:EtOAc 9:1 v/v). $M_p$ 123 °C. IR (ATR): 2927, 2853, 1599, 1582, 1500, 1353, 1312, 1247, 1139, 1085, 885, 837 $cm^{-1}$. $^1H$ NMR (400 MHz, $CDCl_3$) $\delta$ (ppm): 7.97 – 7.89 (m, 4H), 7.88 – 7.82 (m, 2H), 7.03 – 6.97 (m, 2H), 4.04 (t, $J = 6.6$ Hz, 2H), 1.87 – 1.77 (m, 2H), 1.53 – 1.44 (m, 2H), 1.39 – 1.33 (m, 14H), 0.96 – 0.90 (m, 3H).

### 2.2.10. Synthesis of 5-bromo-1-methylindolin-2,3-dione (11a)

5-bromo-1*H*-indol-2,3-dione (7.70 g, 34.1 mmol) was dissolved in anhydrous DMF (25 mL) under nitrogen atmosphere and then $K_2CO_3$ (13.5 g, 97.7 mmol) was added and left stirring for 30 min at room temperature. Afterwards, MeI (3.00 mL, 48.2 mmol) was added and the reaction was stirred overnight. The mixture was diluted with water (ca. 150 mL) and the precipitated was filtered to give **11a** as an orange solid in 95% yield (7.78 g, 32.4 mmol).

$R_f$: 0.33 (Hexane:EtOAc 2:1 v/v). $M_p$ 167 °C. IR (ATR): 2923, 2854, 1720, 1603, 1467, 1439, 1347, 1321, 1170, 1103 $cm^{-1}$. $^1H$ NMR (400 MHz, $CDCl_3$) $\delta$ (ppm): 7.75 – 7.70 (m, 2H), 6.81 (d, $J = 8.9$ Hz, 1H), 3.25 (s, 3H).

### 2.2.11. Synthesis of 5-bromo-1-hexylindolin-2,3-dione (11b)

5-bromo-1*H*-indol-2,3-dione (7.50 g, 33.2 mmol) was dissolved in anhydrous DMF (25 mL) under nitrogen atmosphere and then $K_2CO_3$ (13.1 g, 94.8 mmol) was added and left stirring for 30 min at room temperature. Afterwards, 1-bromohexane (7.00 mL, 49.8 mmol) was added and the reaction was stirred overnight. The mixture was diluted with water (ca. 150 mL) and the precipitated was filtered to give **11b** as an orange solid in 92% yield (9.50 g, 30.6 mmol).

$R_f$: 0.33 (Hexane:EtOAc 2:1 v/v). $M_p$ 105 °C. IR (ATR): 2923, 2855, 1717, 1602, 1460, 1430, 1330, 1312, 1160, 1106 $cm^{-1}$. $^1H$ NMR (400 MHz, $CDCl_3$) $\delta$ (ppm): 7.70 – 7.68 (m, 2H), 6.80 (d, $J = 9.0$ Hz, 1H), 3.70 (t, $J = 7.0$ Hz, 2H), 1.71 – 1.63 (m, 2H), 1.36 – 1.28 (m, 6H), 0.88 (t, $J = 7.0$ Hz, 3H).

### 2.2.12. Synthesis of 5-bromo-1-methylindolin-2-one (12a)

**11a** (2.66 g, 11.1 mmol) was dissolved in hydrazine monohydrate (17.0 mL, 350 mmol) and the solution was refluxed overnight. The crude product was purified by flash column chromatography using a mixture of hexane and EtOAc (10:1 v/v) as the eluent to give **12a** as a pale orange solid in 83% yield (2.08 g, 9.20 mmol).

$R_f$: 0.23 (Hexane:EtOAc 3:1 v/v). $M_p$ 130 °C. IR (ATR): 2920, 2853, 1687, 1608, 1336, 1100, 814, 736, 662 $cm^{-1}$. $^1H$ NMR (400 MHz, $CDCl_3$) $\delta$ (ppm): 7.41 (dd, $J = 8.3$, 1.8, 1H), 7.38 – 7.36 (m, 1H), 6.69 (d, $J = 8.3$ Hz, 1H), 3.52 (s, 2H), 3.19 (s, 3H).

### 2.2.13. Synthesis of 5-bromo-1-methylindolin-2-one (12b)

**11b** (3.50 g, 11.3 mmol) was dissolved in hydrazine monohydrate (17.0 mL, 350 mmol) and the solution was refluxed overnight. The crude product was purified by flash column chromatography using a mixture of hexane and EtOAc (10:1 v/v) as the eluent to give **12b** as a pale white solid in 89% yield (3.00 g, 10.1 mmol).

$R_f$: 0.23 (Hexane:EtOAc 3:1 v/v). $M_p$ 79 °C. IR (ATR): 2924, 2855, 1685, 1600, 1328, 1110, 806, 735, 660 $cm^{-1}$. $^1H$ NMR (400 MHz, $CDCl_3$) $\delta$ (ppm): 7.39 – 7.40 (m, 2H), 6.70 (d, $J = 8.0$ Hz, 1H), 3.67 (t, $J = 7.0$ Hz, 2H), 3.51 (s, 2H), 1.60 – 1.67 (m, 2H), 1.25 – 1.37 (m, 6H), 0.88 (t, $J = 7.0$ Hz, 3H).

### 2.2.14. Synthesis of 3,8,13-trihexyl-5,10,15-trimethyl-10,15-dihydro-5H-diindolo[3,2-a:3′,2′-c]carbazole (13a)

**12a** (1.09 g, 4.82 mmol) and $POCl_3$ (5.00 mL, 51.3 mmol) were mixed and stirred under reflux for 7 h. Then, the mixture was cooled down to room temperature and poured slowly into an ice-water mixture. The solution was neutralized with an aqueous solution of NaOH (1 M).

The obtained solid was separated and washed thoroughly with $CH_2Cl_2$, to give **13a** as a white solid in 51% yield (0.51 g, 0.82 mmol).

$M_p$ 329 °C. IR (ATR): 2924, 2855, 1601, 1571, 1482, 1454, 1437, 1388, 1312, 1243, 1101, 854, 785 $cm^{-1}$. $^1H$ NMR (400 MHz, $CDCl_3$) $\delta$ (ppm): 8.48 (d, $J = 1.8$ Hz, 3H), 7.57 (dd, $J = 8.6$, 1.8 Hz, 3H), 7.46 (d, $J = 8.6$ Hz, 3H), 4.37 (s, 9H).

#### 2.2.15. Synthesis of 3,8,13-trihexyl-5,10,15-trimethyl-10,15-dihydro-5H-diindolo[3,2-a:3′,2′-c]carbazole (13b)

**12b** (3.00 g, 10.1 mmol) and $POCl_3$ (9.00 mL, 92.4 mmol) were mixed and stirred under reflux for 7 h. Then, the mixture was cooled down to room temperature and poured slowly into an ice-water mixture. The solution was neutralized with an aqueous solution of NaOH (1 M). The obtained solid was separated and washed thoroughly with $CH_2Cl_2$, to give **13b** as a white solid in 39% yield (1.10 g, 1.32 mmol).

$M_p$ 204 °C. IR (ATR): 2956, 2924, 2855, 1567, 1467, 1437, 1371, 1313, 1228, 1146, 1114, 848, 785 $cm^{-1}$. $^1H$ NMR (400 MHz, $CDCl_3$) $\delta$ (ppm): 8.27 (d, $J = 1.8$ Hz, 3H), 7.53 (dd, $J = 8.6$, 1.8 Hz, 3H), 7.45 (d, $J = 8.6$ Hz, 3H), 4.68 (t, $J = 8.0$ Hz, 6H), 2.03 – 1.95 (m, 6H), 1.42 – 1.23 (m, 18H), 0.84 (t, $J = 7.0$ Hz, 9H).

#### 2.2.16. Synthesis of 5,10,15-trimethyl-3,8,13-tris(4-((4-(hexyloxy) phenyl)diazenyl) phenyl)-10,15-dihydro-5H-diindolo[3,2-a:3′,2′-c] carbazole (4a)

**13a** (62 mg, 0.10 mmol), **10** (159 mg, 0.39 mmol) and $K_2CO_3$ (77 mg, 0.56 mmol) were dissolved in a mixture of toluene and MeOH (4 mL, 3:1 v/v) under nitrogen atmosphere. Then, $Pd(PPh_3)_4$ (11 mg, 0.01 mmol) was added and the reaction was stirred and refluxed for 24 h. Afterwards, the solvent was removed under reduced pressure. The crude product was purified by flash column chromatography with a mixture of hexane and $CH_2Cl_2$ (1:1 v/v) as the eluent to obtain compound **4a** as an orange solid in 64% yield (79 mg, 0.064 mmol).

$R_f$: 0.15 (Hexane:$CH_2Cl_2$ 1:1 v/v). $M_p$ 216 °C. IR (ATR): 2922, 2855, 1595, 1579, 1497, 1474, 1314, 1242, 1150, 1098, 1027, 1006, 842, 800, 772, 731 $cm^{-1}$. $^1H$ NMR (400 MHz, $CDCl_3$) $\delta$ (ppm): 8.69 (d, $J = 1.7$ Hz, 3H), 8.08 – 8.03 (m, 6H), 8.00 – 7.94 (m, 6H), 7.93 – 7.87 (m, 6H), 7.78 (dd, $J = 8.4$, 1.7 Hz, 3H), 7.61 (d, $J = 8.4$ Hz, 3H), 7.06 – 7.01 (m, 6H), 4.48 (s, 9H), 4.07 (t, $J = 6.6$ Hz, 6H), 1.89 – 1.79 (m, 6H), 1.54 – 1.45 (m, 6H), 1.44 – 1.33 (m, 12H), 0.91 – 0.81 (m, 9H). $^{13}C$ NMR (101 MHz, $CDCl_3$) $\delta$ (ppm): 161.6, 151.4, 147.1, 144.4, 141.5, 139.2, 131.9, 127.7 (2C), 124.8 (2C), 124.5, 123.3 (2C), 122.4, 120.4, 115.7, 114.8 (2C), 109.9, 35.9, 31.6, 29.7, 29.2, 25.8, 22.7, 14.0. MS (MALDI-TOF) *m/z*: calcd. for $C_{81}H_{81}N_9O_3$ $(M)^{\cdot+}$, 1227.6; found 1227.6.

#### 2.2.17. Synthesis of 5,10,15-trihexyl-3,8,13-tris(4-((4-(hexyloxy)phenyl) diazenyl) phenyl)-10,15-dihydro-5H-diindolo[3,2-a:3′,2′-c]carbazole (4b)

**13b** (100 mg, 0.12 mmol), **10** (179 mg, 0.44 mmol) and $K_2CO_3$ (93 mg, 0.67 mmol) were dissolved in a mixture of toluene and MeOH (4 mL, 3:1 v/v) under nitrogen atmosphere. Then, $Pd(PPh_3)_4$ (6.35 mg, 0.005 mmol) was added and the reaction was stirred and refluxed for 24 h. Afterwards, the solvent was removed under reduced pressure. The crude product was purified by flash column chromatography with a mixture of hexane and $CH_2Cl_2$ (2:1 v/v) as the eluent to obtain compound **4b** as an orange solid in 51% yield (88 mg, 0.061 mmol).

$R_f$: 0.31 (Hexane:$CH_2Cl_2$ 1:1 v/v). $M_p$ 131 °C. IR (ATR): 2922, 2851, 1595, 1582, 1560, 1498, 1472, 1318, 1243, 1191, 1152, 1105, 1027, 997, 842, 796, 773, 725 $cm^{-1}$. $^1H$ NMR (400 MHz, $CDCl_3$) $\delta$ (ppm): 8.08 – 8.00 (m, 6H), 7.98 – 7.94 (m, 6H), 7.90 – 7.86 (m, 6H), 7.74 (d, $J = 8.4$ Hz, 3H), 7.71 (d, $J = 8.4$ Hz, 3H), 7.04 (d, $J = 9.0$ Hz, 6H), 4.97 (t, $J = 8.0$ Hz, 6H), 4.07 (t, $J = 6.6$ Hz, 6H), 2.17 – 2.00 (m, 6H), 1.89 – 1.78 (m, 6H), 1.54 – 1.44 (m, 6H), 1.42 – 1.19 (m, 12H), 1.18 – 1.04 (m, 6H), 0.99 – 0.80 (m, 18H), 0.74 (t, $J = 7.2$ Hz, 9H). $^{13}C$ NMR (101 MHz, $CDCl_3$) $\delta$ (ppm): 161.6, 151.4, 147.1, 144.6, 140.9, 139.5, 132.5, 127.9 (2C), 124.7 (2C), 124.0, 123.2 (2C), 122.6, 120.4, 114.7 (2C), 110.8, 103.5, 68.4, 47.4, 31.6, 30.2, 29.7, 29.2, 26.6, 25.7, 22.6 (2C), 14.0 (2C). MS (MALDI-TOF) *m/z*: calcd. for $C_{96}H_{112}N_9O_3$ $(M + H)^+$, 1438.9; found 1438.8.

## 3. Results and discussion

### 3.1. Synthesis and molecular design

As stated, two classes of triindole-AB derivatives were designed (Fig. 2). In the *N*-AB-triindoles (**1**–**3**), the AB moieties were tethered to the triindole core via alkyl spacers to electronically decouple the photochromic and OSC domains, thereby preserving the individual functionalities while enhancing solubility [19]. One to three AB units were integrated, with the remaining nitrogen atoms alkylated with either methyl (a) or hexyl (b) groups to emulate the substitution patterns of high-performing p-type OSCs of *N*-trimethyltriindole (TMT) and *N*-trihexyltriindole (THT) [17,20,21]. In contrast, the *C*-AB-triindoles featured direct covalent bonding of the AB units at the 3,8,13 positions of the triindole core to extend π-conjugation, while peripheral alkyl chains on the triindole nitrogen atoms and the 4' position of the AB units ensured better processability.

Previously, the hexyloxyderivative AB **5** and THT units were synthesized as appropriate models to ease comparison of their spectroscopic and kinetic properties with those of the final AB-triindole systems. The synthesis of these compounds were prepared following a literature procedure [20,22].

The synthetic route for the *N*-AB-triindoles was established by coupling AB halide **6** with triindole **7** to prepare mono- (**1**) di- (**2**) or tri-AB units (**3**) (Scheme 1). Compound **6** was obtained from 4-phenylazophenol via a Mitsunobu reaction under standard conditions, while 2-oxindole under $POCl_3$ afforded **7** as reported conditions [20]. The final *N*-AB-triindoles compounds **1**–**3** were obtained and isolated by a nucleophilic substitution in a two-step process. The first step (reaction iii) consisted of an N-alkylation between **6** and **7** and the subsequent second step (reaction iv) involved the alkylation of the remaining NH positions with MeI (**1a, 2a**) or 1-bromohexane (**1b, 2b**).

Reagents and conditions: i) 6-bromo-1-hexanol, $PPh_3$, DIAD, dry THF, rt; ii) $POCl_3$, Δ; iii) **6**, NaH, anh. DMF, 100 °C (see Table 1); iv) MeI (**1a**, **2a**) or 1-bromohexane (**1b**, **2b**), NaH, anh. DMF, 100 °C.

Furthermore, the key substitution step (reaction iii) exhibited limited selectivity, yielding mixtures of mono-, di- and tri-AB-substituted products. Although complete selectivity of mono- or di-substitution

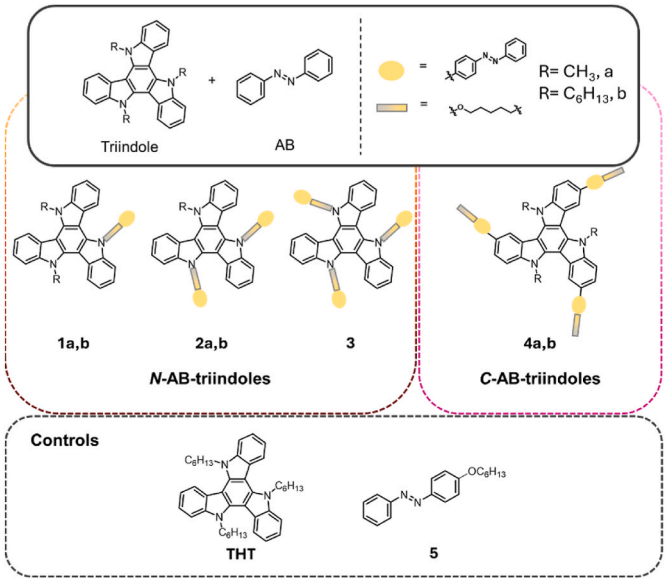


**Fig. 2.** Schematic representation of *N*-(**1**–**3**) and *C*-AB-triindole (**4**) derivates studied within this work and the control compounds (*N*-trihexyltriindole, THT and **5**).

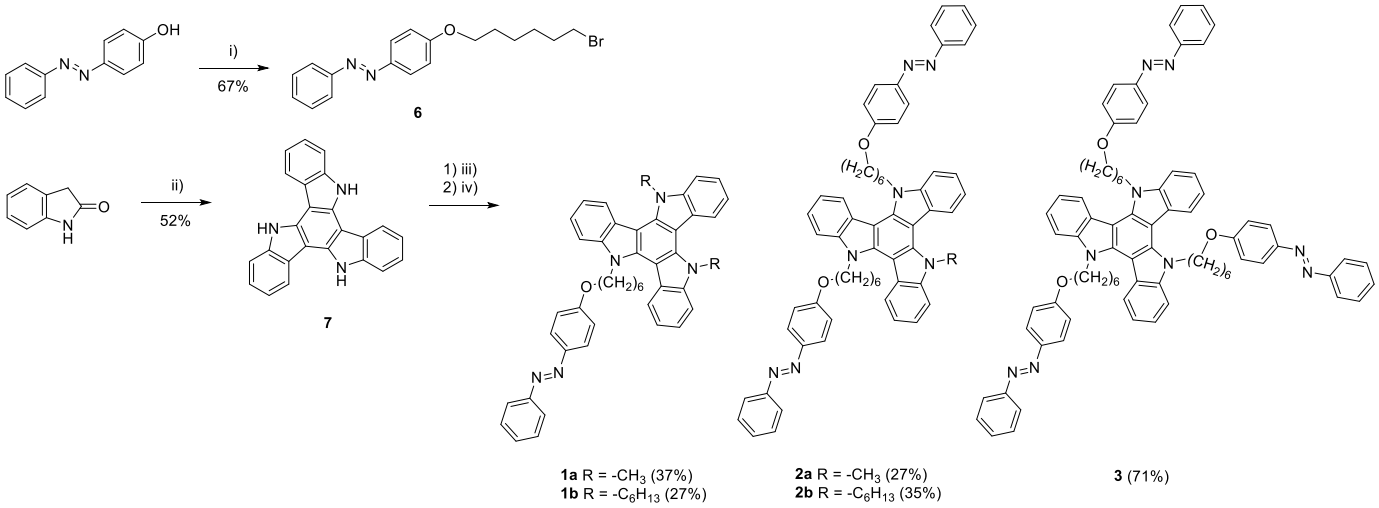


**Scheme 1.** Synthetic route of *N*-AB-substituted triindole compounds **1a**−**b**, **2a**−**b**, **3**.

**Table 1**
Optimization of the reaction conditions for the formation of AB-triindole derivatives **1**–**3** (reaction iii).

| Entry | R–[a] | 7 (eq.) | NaH (eq.) | 6 (eq.) | Yield 1 (%) | Yield 2 (%) | Yield 3 (%) | molar ratio 1:2:3 |
|---|---|---|---|---|---|---|---|---|
| 1 (a) | $CH_3$ | 1 | 3.1 | 1.1 | 37 | 24 | 3 | 1:0.6:0.1 |
| 2 (b) | $C_6H_{13}$ | 1 | 3.1 | 1.1 | 27 | 26 | 5 | 1:0.96:0.2 |
| 3 (a) | $CH_3$ | 1 | 4.1 | 2.1 | 17 | 27 | 32 | 0.6:1:1.2 |
| 4 (b) | $C_6H_{13}$ | 1 | 4.1 | 2.1 | 14 | 35 | 41 | 0.4:1:1.2 |
| 5 | (−)[b] | 1 | 6.1 | 6.1 | 0 | 0 | 71 | 0:0:1 |

[a] Alkyl groups attached in the remaining NH positions in reaction iv.
[b] Not proceeded.

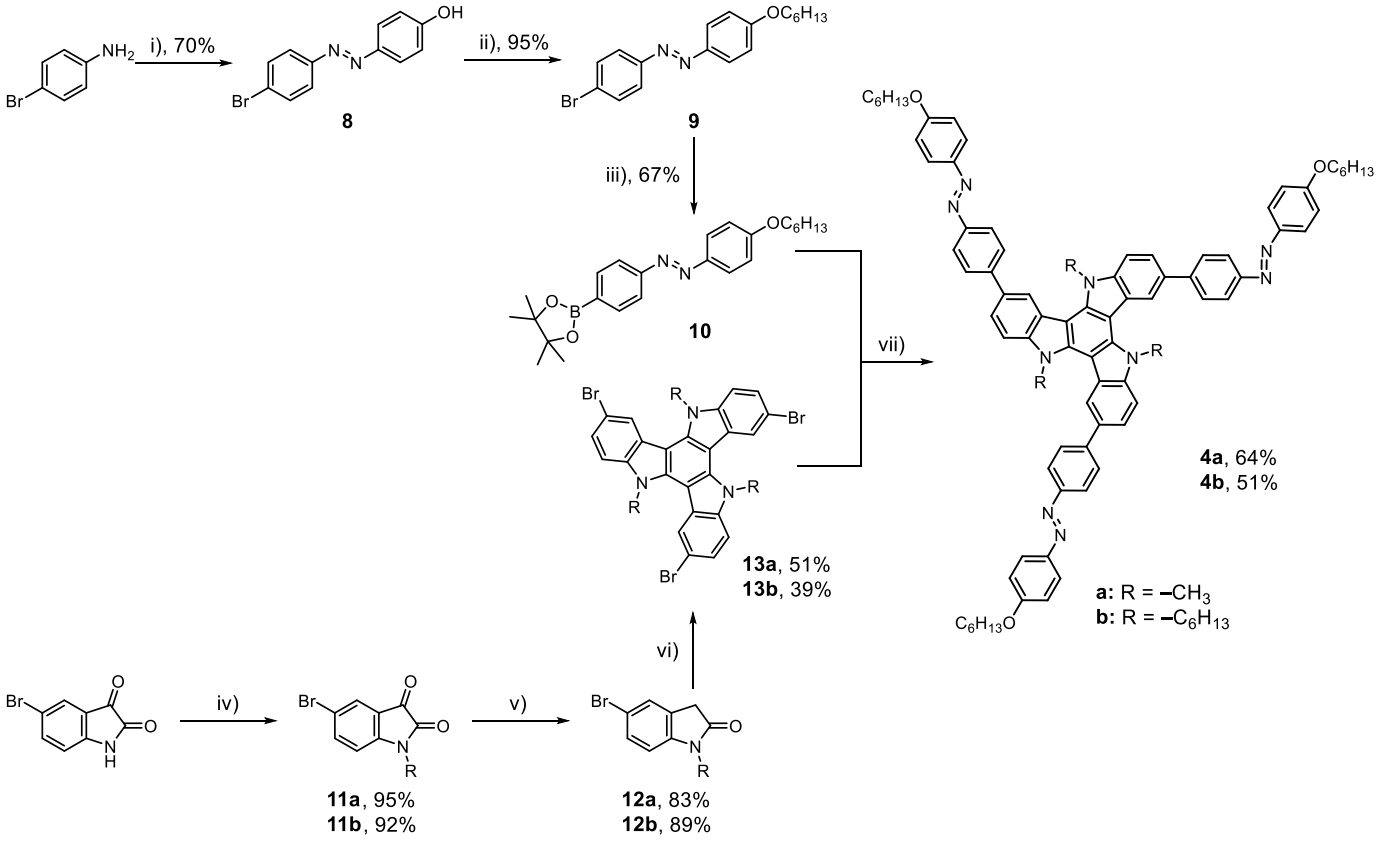


**Scheme 2.** Synthetic route of *C*-AB-substituted triindole compounds **4a,b**.

could not be achieved, the product distribution could be steered by adjusting the reagent stoichiometry (Table 1). In this manner, using 3.1 eq. NaH and 1.1 eq. of **6** favored the mono-AB substitution, affording **1a** and **1b** in 37% and 27% yield, respectively (Table 1, Entries 1,2), while raising the loadings to 4.1 eq. of NaH and 2.1 eq. of **6** promoted the di-AB substitution to give **2a** (27%) and **2b** (35%) (Table 1, Entries 3,4). In contrast, employing a large excess of both reagents (6.1 eq.) led to the selective formation of the tri-AB substituted derivative **3** in 71% yield (Table 1, Entry 5). An expanded table with the optimization experiments for reaction iii) is reported in the Supplementary data (Table S1).

For the synthesis of the *C*-AB-triindoles **4a,b**, the selected strategy involved a Suzuki-Miyaura C–C cross-coupling reaction between a tri-brominated triindole core and a boronic ester-functionalized AB (Scheme 2). For the AB unit, starting from 4-bromoaniline, the corresponding azophenol **8** was synthesized via a diazotization with $NaNO_2$, followed by a coupling with phenol to obtain the azobenzene moiety. Then, O-alkylation with 1-bromohexane was used to yield compound **9**. Subsequent palladium-catalyzed Suzuki-Miyaura borylation, following a modified literature procedure [23], afforded the pinacol boronic ester derivative **10** in a 67% yield. In parallel, for the triindole fragment, N-alkylation of commercially available 5-bromoisatin with a methyl (**11a**) or a hexyl chain (**11b**), followed by a Wolff-Kishner reduction (**12a,b**) and polycondensation with $POCl_3$ yielded the tribrominated-substituted triindole derivatives **13a,b**. Finally, the Suzuki-Miyaura cross-coupling of AB **9** with triindole **13a,b** furnished the target *C*-azo-triindoles **4a,b** in moderate yields, above 50%. Overall, the full synthetic route encompassed seven steps, resulting in 26% overall yield for **4a**, and slightly lower, 16%, for **4b**.

Reagents and conditions: i) 1) $NaNO_2$, HCl, $H_2O$, 0 °C and 2) Phenol, NaOH, $H_2O$, 0 °C; ii) $K_2CO_3$, $C_6H_{13}Br$, DMF anh., rt; iii) $B_2pin_2$, KOAc, Pd$(PPh_3)_2Cl_2$, toluene, Δ; iv) $K_2CO_3$, MeI, DMF anh., rt; v) $NH_2NH_2{\cdot}H_2O$, Δ; vi) $POCl_3$, Δ; vii) $K_2CO_3$, Pd$(PPh_3)_4$, toluene:MeOH (3:1 v/v), Δ.

### 3.2. Optical properties

The optical properties of the compounds were first investigated by UV-Vis spectroscopy in dilute solutions of toluene (10 μM). As expected, *N*-AB-triindole compounds **1**–**3** displayed absorption spectra that closely resemble the superposition of the control compounds THT and AB **5**, evidencing that the hexyl spacer effectively decouples the AB and triindole units electronically (Fig. 3a). Specifically, these compounds exhibited sharp absorption peaks in the near UV region coming from the triindole unit (319, 338 and 353 nm), with the broadening of the highest-wavelength peak attributed to the overlap with the symmetry-allowed π-π* transition of the *p*-alkoxy-substituted AB moiety. Additionally, a weaker and broad absorption band between 430 and 450 nm was visible, corresponding to the symmetry forbidden n-π* transition of the AB unit. Furthermore, increasing the number of AB units in the molecule led to a proportional increase in the overall absorption intensity and the molar absorption coefficients (Table S2). In contrast, the absorption spectrum of solid films of **1a** showed both a bathochromic shift of the main peaks to 328, 345 and 358 nm and a much weaker response, consistent with the aggregation and the expected steric hindrance in the solid state for the *trans-cis* configuration (Fig. S1) [24].

In contrast, the *C*-AB-triindole derivatives **4a,b** showed a markedly different absorption profile (Fig. 3b). A broader and more red-shifted band centered at 370 nm was observed, reflecting an extended conjugation between the triindole and AB moieties and their resulting electronic interaction.

#### 3.2.1. Photoisomerization behavior

The light-driven switching behavior of mono-AB-substituted *N*-AB-triindole compound **1a**, *C*-AB-triindole compound **4a** and the control compound **5** was rigorously studied under different light inputs by UV-Vis spectroscopy in both solution and solid samples. Upon UV irradiation (365 nm) of **1a** in toluene solution (10 μM), initially dominated by the *trans* isomer, a *cis*-enriched photostationary state (PSS) is rapidly reached within 5 s, corresponding to a nearly complete *trans*-to-*cis* conversion (Fig. 4a). The occurrence of this photoisomerization was also qualitatively confirmed by $^1H$ NMR spectroscopy (Figs. S2 and S3). This isomerization is manifested by a significant decrease in the absorption at ca. 350 nm and a concomitant slight increase at 450 nm of the π-π* and n-π* transitions of the AB moiety, respectively, while the triindole electronic profile remains essentially unchanged. This process is also accompanied by a visible color change of the solution from yellowish-orange (ca. 430 nm) to a deeper orange hue (ca. 460 nm). (Fig. 4b, inset image). Subsequent back-isomerization to the *trans* configuration was triggered by different visible light sources: green light (520 nm) proved to be more effective than blue light (450 nm), affording a PSS that more closely resembled the initial absorption profile. This behavior is consistent with the lower photon energy of green light, which minimizes re-excitation to the *cis* isomer. These results also correlated to the photoisomerization behavior of the control compound **5**, which reached a *cis* population of 96% upon UV irradiation and decreased to 26% and 14% in the PSS at 450 and 510 nm, respectively, further proving the electronic decoupling between the AB and the triindole units (Fig. S4). Extending the study to the solid state, a drop-casted film of **1a** was deposited on a quartz substrate and irradiated analogously to the solution sample. The film displayed spectral responses consistent with those observed in dilute solution, thereby confirming the retention of the photoresponsive behavior in the solid state for such photochromic systems (Fig. S5).

In contrast, for compound *C*-AB-triindole **4a**, UV light did not induce a *trans*-to-*cis* photoisomerization due to the red-shifted π-π* transition from the extended π-conjugation (Fig. 4c). Instead, a change in the absorption profile was efficiently induced by irradiating the sample with blue light (410 nm), which caused a decrease of absorption in the region

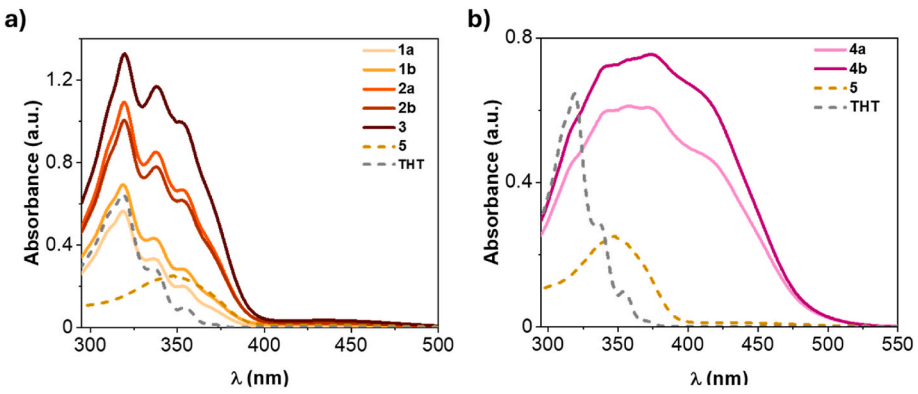


**Fig. 3.** UV-Vis spectra in toluene solution (10 μM) of the control compounds **5** and *N*-trihexyltriindole (THT) with compounds a) **1**–**3** and b) **4**.

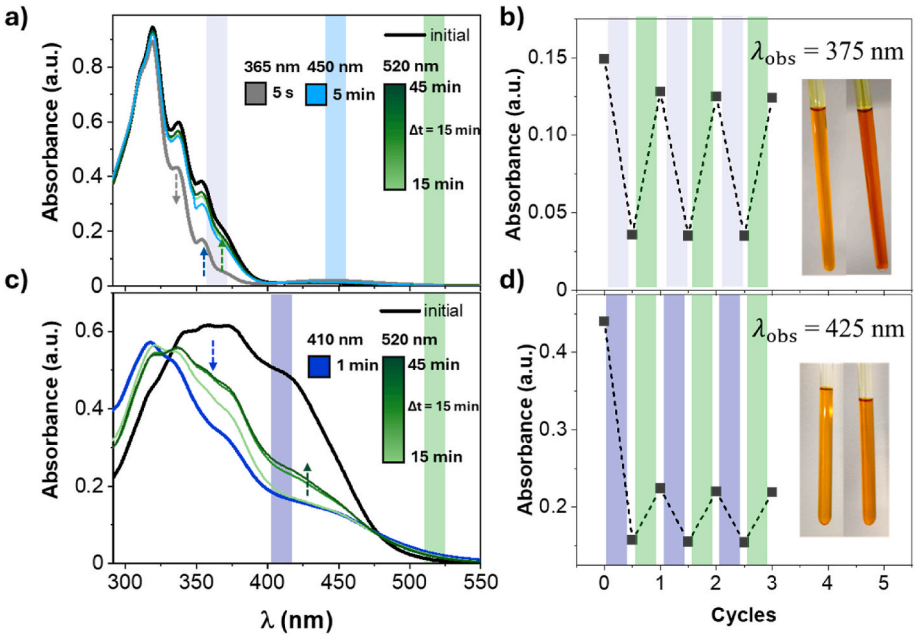


**Fig. 4.** UV-Vis spectra of a) **1a** and c) **4a** (10 μM in toluene) before irradiation (black) and after light-induced *trans* → *cis* (365 or 410 nm) and subsequent *cis* → *trans* (450 or 520 nm) photoisomerization. Arrows indicate the direction of the absorbance change, while shaded regions and lines denote the irradiation wavelengths used. b,d) Corresponding photoswitching cycles of b) **1a** and d) **4a** monitored at the indicated $\lambda_{obs}$. Inset images show solutions before (left) and after (right) irradiation with 365 or 410 nm light.

350–450 nm and an increase at 500 nm, again, consistent with a *trans*-to-*cis* isomerization process. Photoreversion to the *trans* isomer was accomplished upon green light irradiation (520 nm), although this process was less efficient than in **1a**, likely due to the reduced spectral separation between the π-π* and n-π* transitions from the extended conjugation, limiting spectral selectivity [7,25,26]. This is a well-known challenge associated with the integration of AB units into conjugated systems, which could be mitigated through chemical fine-tuning of the AB moiety, such as by introducing *ortho*-halogen substituents to improve the spectral separation between the *trans* and *cis* isomer [27–29]. This

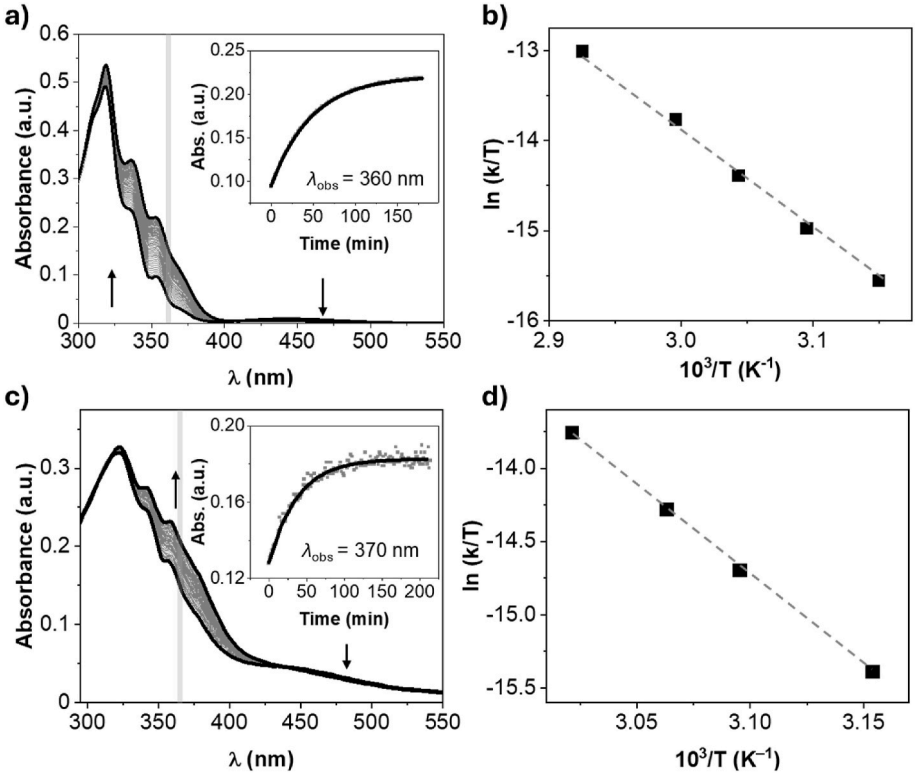


**Fig. 5.** Kinetic study for compound **1a**. Time-resolved UV-Vis spectra at 60 °C a) in toluene (10 μM) and c) in solid state. The arrows denote the evolution of absorbance with time. The inset represents the absorbance at the observed wavelength (grey area, $\lambda_{obs}$ = 360 nm) vs. time and the fitting (black line). b,d) ln (k/T) vs 1/T representation and the fitting (dotted line) for *k* values obtained at 40–60 °C. b) In toluene (10 μM) and d) in solid state.

would enable more selective excitation of each state using different irradiation wavelengths.

Furthermore, the reversibility and robustness of the photoswitching behavior of these materials were confirmed by performing three consecutive switching cycles using alternating irradiation at the appropriate wavelengths (Fig. 4b–d). More specifically, isomerization to the *cis* isomer was induced using UV light for **1a**, or 410 nm light for **4a** and 520 nm light for their back-conversions.

#### 3.2.2. *Cis-to-trans thermal relaxation and bistability*

The thermal *cis*-to-*trans* back-isomerization was investigated using time-resolved UV-Vis spectroscopy in dilute solution of toluene (10 μm; Fig. 5a and Fig. S6a–S10a) or in solid state for **1a** (Fig. 5c). The half-lives ($t_{1/2}$) were determined by fitting the absorbance vs. time to a mono-exponential decay model at elevated temperatures (40–60 °C) and extrapolated to the room temperature value from an Arrhenius plot (Fig. 5b–d and Fig. S6b–S12b). Additionally, the variation of the rate constants with the temperature allowed also the determination of the enthalpies and entropies of activation ($\Delta H^{\ddagger}$ and $\Delta S^{\ddagger}$, respectively), which are collected in Table 2.

All compounds exhibited two distinct isosbestic points: at 303 and 407 nm for *N*-AB-triindoles **1**–**3** (Fig. 5a, Fig. S7a–S10a) and at 331 and 478 nm for C-AB-triindoles **4** (Figs. S11a and S12a), indicating a clean *trans-cis* interconversion without formation of side products. Additionally, the *cis*-to-*trans* thermal relaxation $t_{1/2}$ values were observed to be in the hour scale, as observed for alkoxy-substituted ABs [12]. In particular, in the *N*-AB-triindole series a clear inverse correlation was observed between molecular volume and relaxation rate. In this manner, smaller derivatives such as **1a,b** and **2a** exhibited $t_{1/2}$ values around 34–39 h and activation parameters similar to the control compound **5** ($t_{1/2} = 39$ h). By replacing methyl with hexyl groups in di-substituted AB derivative **2b** reduced the $t_{1/2}$ to 23 h, while the addition of an extra AB unit in derivative **3** showed a twofold faster *cis*-to-*trans* thermal relaxation than the mono-substituted AB analogues **1** ($t_{1/2} = 18$ h vs 39 h for **1a**). This acceleration is attributed to an increased steric hindrance introduced in the *cis* configuration, which destabilizes this isomer and promotes reversion to the *trans* configuration. This effect is reflected in a more considerable negative $\Delta S^{\ddagger}$ (−92 vs. −28 J mol$^{-1}$ K$^{-1}$) and a lower $\Delta H^{\ddagger}$ (96 vs. 75 kJ mol$^{-1}$) for **3** compared to **5**, indicating a more ordered and less energetic transition state for the former. A similar behavior was observed when comparing **1a** in dilute solution to its solid-state form on a quartz substrate, which showed similar $t_{1/2}$ values (37 h). However, the film exhibited higher $\Delta H^{\ddagger}$ and, notably, an $\Delta S^{\ddagger}$ close to zero (−3 J mol$^{-1}$ K$^{-1}$), suggesting a more constrained environment during isomerization in the solid state.

Conversely, *C*-AB-triindoles **4a,b** showed significantly faster thermal relaxation half-lives ($t_{1/2} \approx 6$–7 h) than the *N*-AB-triindoles, ascribed to the extended aromatic conjugation in these [30–32]. Despite this, their thermal activation parameters remained comparable to those of **5**.

**Table 2**
Kinetic and thermal activation parameters at 25 °C of compounds **1**–**5** in toluene (10 μM) obtained from the Eyring plots.

| | $k$ (s$^{-1}$)[a] × 10$^{-6}$ | $t_{1/2}$ (h)[b] | $\Delta H^{\ddagger}$ (kJ mol$^{-1}$)[c] | $\Delta S^{\ddagger}$ (J mol$^{-1}$ K$^{-1}$)[d] |
|---|---|---|---|---|
| **5** | 5.0 | 39 | 96.7 ± 0.1 | −28.2 ± 0.4 |
| **1a** | 5.0 | 39 | 96 ± 2 | −28 ± 6 |
| | 5.2[e] | 37 | 103 ± 1 | −3 ± 2 |
| **1b** | 5.7 | 34 | 93 ± 1 | −37 ± 2 |
| **2a** | 5.6 | 34 | 94 ± 3 | −33 ± 8 |
| **2b** | 8.3 | 23 | 81 ± 1 | −72 ± 1 |
| **3** | 11 | 18 | 75 ± 1 | −92 ± 1 |
| **4a** | 28 | 6.8 | 93 ± 1 | −22 ± 4 |
| **4b** | 30 | 6.3 | 90 ± 1 | −33 ± 4 |

[a] Constant rate at room temperature.
[b] Half-live at room temperature.
[c] Enthalpy of activation and.
[d] Entropy of activation.
[e] Values from a drop-casted film of **1a** on a quartz substrate.

### 3.3. *Thermal stability and electronic energy levels*

The thermal properties and the frontier energy levels of the AB-triindole compounds **1**–**4** were measured and compared to the control compounds for triindole (THT) and AB (**5**) subunits. The summary of all the data is found in Table 3.

Thermal stability was assessed by evaluating the decomposition temperature ($T_d$) of the compounds, as determined through thermogravimetric analysis (TGA; Fig. S13). All compounds exhibited $T_d$ values above 340 °C, which are substantially higher than those of the individual units **5** (225 °C) [33] and THT (301 °C) [20]. This substantial thermal stability is critical for various deposition techniques in electronic devices, ensuring the integrity and performance of the resulting materials [34,35].

For the frontier energy levels of the AB-triindole derivatives, the ionization potentials (IPs) were determined from cyclic voltammetry (CV; $IP_{CV}$) in $CH_2Cl_2$ (1 mM) and photoemission spectra (PES; $IP_{PE}$) in pristine films, which are schematically illustrated in Fig. 6. For the former, profiles of the studied AB-triindole compounds exhibited a quasi-reversible oxidation process attributed to the triindole core, together with an irreversible reduction typical of AB derivatives (Fig. S14) [36]. $IP_{CV}$ values extracted from the oxidation onset revealed that all the studied AB-triindole derivatives showed values closely matching to the reference compound THT, which hovered around 5.60 eV. These values are ideal for hole-transporting materials and simultaneously provide stability against oxidative doping from atmospheric oxygen [37,38]. In parallel, PES measurements yielded slightly lower $IP_{PE}$ values (5.00–5.15 eV; Fig. S15), which indicated an improved energetic alignment for hole injection with common metal electrodes used in electronic devices (e.g., 5.1 eV work function for Au contacts). This discrepancy between the $IP_{CV}$ and $IP_{PE}$ values could arise from the differences in intermolecular interactions present in the solid state versus in dilute solution, which were also reflected in the UV-Vis spectra. Additionally, the optical energy bandgap ($E_{gap}^{opt}$) were estimated from the onset wavelength ($\lambda_{abs,onset}$) of the absorption spectra. In this case, *N*-AB-triindoles **1**–**3** showed values slightly lower but similar to that of THT (3.53 eV), while *C*-AB-triindoles **4a,b** exhibited a considerable reduced $E_{gap}^{opt}$ (2.95 eV), consistent with the extended π-conjugation between the triindole and AB units.

Hence, the prepared and studied AB-triindole compounds **1**–**4** overall combined thermal robustness with appropriate frontier energy levels, showing their clear potential as air-stable p-type OSCs.

### 3.4. *Charge transport properties (time-of-flight)*

The charge-transport properties of the whole family of AB-triindole compounds **1**–**4** were assessed using TOF measurements by sandwiching the organic layer (d > 1 μm) in diode-like devices consisting of an ITO-coated glass substrate and an aluminum electrode (see Table 4) (Fig. S16).

The measured hole drift mobilities exhibited a linear dependence on the square root of the applied electric field, consistent with a hopping transport mechanism (Figs. S16 and S17) [39]. Among the studied pristine films, the hexyl-substituted mono-AB derivative **1b** displayed the highest performance, with $\mu_h$ of 1.5 × 10$^{-4}$ cm$^2$ V$^{-1}$ s$^{-1}$ under an applied electric field of 5.6 × 10$^5$ V cm$^{-1}$, amounting to an order of magnitude higher than its methyl analogue **1a** ($\mu_h = 1.7 \times 10^{-5}$ cm$^2$ V$^{-1}$ s$^{-1}$). However, pristine films of compounds **2**–**4** exhibited poor structural quality and resulted in devices that were inoperative for TOF analysis. Consequently, blends with an inert polymer host, bisphenol Z-polycarbonate (PC-Z) at a 1:1 wt ratio were employed to improve film formation [40,41]. Under these conditions, the obtained $\mu_h$ values for

**Table 3**
Thermal and electrochemical properties of *N*-trihexyltriindole (THT) and **1**–**5**.

| | $T_d$ (°C)[a] | $\lambda_{abs,onset}$ (nm)[b] | $E_{gap}^{opt}$ (eV)[c] | $E^{cat}$ (V)[d] | $E_{onset}^{ox}$ (V)[e] | $IP_{CV}$ (eV)[f] | EA (eV)[g] | $IP_{PE}$ (eV)[h] |
|---|---|---|---|---|---|---|---|---|
| **5** | 225[i] | (–)[j] | (–)[j] | −2.01 | (–)[j] | (–)[j] | (–)[j] | (–)[j] |
| THT[k] | 301 | 351 | 3.53 | (–)[l] | 0.21 | 5.60 | 2.07 | 4.79 |
| **1a** | 359 | 352 | 3.52 | −1.98 | 0.22 | 5.61 | 2.08 | 5.11 |
| **1b** | 363 | 354 | 3.50 | −2.01 | 0.24 | 5.63 | 2.14 | 5.13 |
| **2a** | 360 | 355 | 3.49 | −2.01 | 0.24 | 5.63 | 2.12 | 5.08 |
| **2b** | 350 | 354 | 3.50 | −2.03 | 0.25 | 5.64 | 2.13 | 5.07 |
| **3** | 343 | 354 | 3.50 | −2.05 | 0.25 | 5.64 | 2.13 | 5.04 |
| **4a** | 331 | 420 | 2.95 | −2.05 | 0.21 | 5.60 | 2.65 | 5.03 |
| **4b** | 333 | 420 | 2.95 | −2.01 | 0.27 | 5.66 | 2.76 | 4.99 |

[a] Decomposition temperature at a 5% weight loss.
[b] Absorption onset wavelength.
[c] Optical energy gap estimated from the absorption spectrum.
[d] Reduction potential vs. $Fc^+/Fc$.
[e] Onset oxidation potential vs. $Fc^+/Fc$.
[f] Ionization potential extracted from the cyclic voltammetry ($E_{onset}^{ox}$).
[g] Electron affinity.
[h] Ionization potential extracted from the photoemission spectra.
[i] Ref. [33].
[j] Not measured.
[k] Ref. [20].
[l] Not detected.

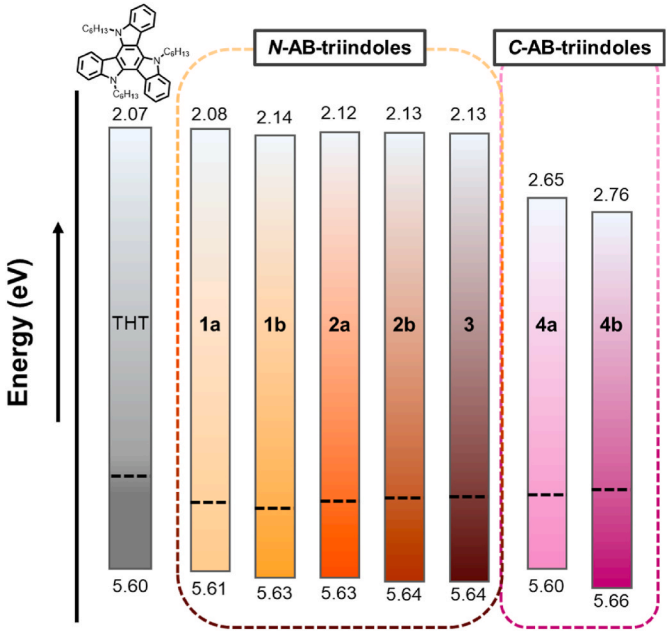


**Fig. 6.** Schematic representation of frontier energy levels of compounds **1**–**4** and *N*-trihexyltriindole (THT), showing the HOMO/LUMO energies extracted from cyclic voltammetry and HOMO energy values from photoemission spectroscopy (dotted lines).

the *N*-AB-triindoles **1a** and **1b** decreased by approximately two orders of magnitudes relative to their pristine films, yielding values of $1.1\times 10^{-7}$ and $3.3 \times 10^{-6}$ $cm^2\ V^{-1}\ s^{-1}$, respectively. In particular, the mobility obtained for **1b** fell within the range reported for some structurally related *N*-alkyl-substituted triindoles measured under comparable film preparation and electric field conditions [42]. This is particularly significant given that **1b** incorporated a photoactive AB chromophore, which is typically inactive with respect to charge transport. Hence, the preservation of meaningful hole mobility upon the incorporation of a single AB unit, while simultaneously imparting photoresponsive functionality, highlights the exceptional balance of both properties achieved in these AB-triindole hybrids. In contrast, increasing the degree of AB substitution progressively compromised the charge transport:

**Table 4**
Hole mobility parameters of vacuum-evaporated pristine films of **1a,b** and drop-casted PC-Z doped with compounds **1**–**4** (1:1 w/w) on ITO-coated glass substrates.

| | $\mu_h$ ($cm^2\ V^{-1}\ s^{-1}$)[a] | $\mu_0$ ($cm^2\ V^{-1}\ s^{-1}$)[b] | $\alpha$ ($cm^{1/2}\ V^{-1/2}$)[c] |
|---|---|---|---|
| **1a** | $1.7 \times 10^{-5}$ | $2.0 \times 10^{-7}$ | 0.0059 |
| **1b** | $1.5 \times 10^{-4}$ | $1.2 \times 10^{-7}$ | 0.0093 |
| **1a + P**[d] | $1.1 \times 10^{-7}$ | $8.3 \times 10^{-8}$ | 0.0030 |
| **1b + P** | $3.3 \times 10^{-6}$ | $3.2 \times 10^{-12}$ | 0.0246 |
| **2a + P** | $7.2 \times 10^{-8}$ | $2.7 \times 10^{-10}$ | 0.0067 |
| **2b + P** | $3.3 \times 10^{-8}$ | $3.1 \times 10^{-9}$ | 0.0058 |
| **3 + P** | (–)[e] | (–)[e] | (–)[e] |
| **4a + P** | $6.4 \times 10^{-5}$ | $8.0 \times 10^{-7}$ | 0.0057 |
| **4b + P** | $1.4 \times 10^{-5}$ | $2.3 \times 10^{-6}$ | 0.0026 |

[a] Hole mobilities measured at an applied electric field $6 \times 10^5$ V $cm^{-1}$.
[b] Zero-field mobility.
[c] Field dependence parameter.
[d] Bisphenol Z-polycarbonate (1:1 w/w).
[e] Not operative.

disubstituted-AB derivatives **2a** and **2b** exhibited mobilities below $10^{-7}$ $cm^2\ V^{-1}\ s^{-1}$ in PC-Z doped films, while the trisubstituted analogue **3** showed no detectable transient signal, even within the host matrix. This trend indicated that although limited AB incorporation was tolerated, higher substitution became detrimental to charge transport within the *N*-AB-triindole system.

Remarkably, a different behavior was observed for the *C*-azo-triindoles **4a,b**, which displayed noticeably enhanced mobilities in PC-Z doped films compared to **1a,b**. Specifically, the methylated **4a** reached mobilities of $6.4 \times 10^{-5}$ $cm^2\ V^{-1}\ s^{-1}$ and the hexylated **4b** of $1.4 \times 10^{-5}$ $cm^2\ V^{-1}\ s^{-1}$, which corresponded to an order of magnitude higher than **1b** under the same deposition conditions and applied electric field. Thus, these results suggest that both extended π-conjugation and the AB linkage position at the carbon rather than nitrogen is advantageous for facilitating hole transport. Indeed, reported photoactive OSC-AB hybrids share this architecture, with the AB aromatic core directly attached to the OSC framework [15,16].

Altogether, these findings highlight the considerable potential of AB-triindole derivatives as photoactive OSCs. In particular, the pristine film of mono-substituted *N*-AB-triindole **1b** demonstrated the highest mobility overall ($1.5 \times 10^{-4}$ $cm^2\ V^{-1}\ s^{-1}$), comparable to that of analogous N-alkylated triindoles. In contrast, *C*-AB-triindole derivatives **4a,**

**b** could only be measured in a PC-Z polymer blend, where they outperformed the N-linked derivatives under those blended conditions. Hence, strategic π-extension in C-linked AB-triindole derivatives further enhanced charge transport through improved conjugation. Despite the clear trends in hole mobility revealed by the TOF measurements, this technique intrinsically requires photoexcitation using a UV laser pulse ($\lambda_{Ex}$ = 355 nm) to generate the charge-carrier sheet, which inevitably induces a certain degree of photoisomerization during the measurements. In particular, such irradiation to the *N*-AB-triindole films is expected to promote *trans*-to-*cis* isomerization to a significant extent, whereas in films based on *C*-AB-triindole derivatives this process is scarcely present due to the red-shifted π-π* transition of the extended π-conjugation, in agreement with the UV-Vis photoisomerization studies. Consequently, the measured mobilities cannot be assigned to a pure *trans* or *cis* states but to the transient population originated under the photoinduced perturbation. Nevertheless, these results demonstrate that incorporation of the AB unit does not suppress hole transport and thus support the proof-of-concept character of these compounds as light-responsive semiconductors. Future studies aimed at disentangling the charge transport properties of the *trans* and *cis* isomers will be explored by using methodologies that does not rely on optical excitation, such as space-charge-limited current (SCLC) or field-effect transistor (FET) devices.

### 3.5. Solid-crystal structures and molecular packing

In order to unlock the role of AB units the interaction with the triindole core in the solid state, the packing arrangement of *N*-methylated-monosubstituted-AB-triindole **1a** and the analogue disubstituted-AB **2a** were elucidated from appropriate single crystals evaporated from a solution of ethanol:$CH_2Cl_2$ (1:1 v/v) and hexane:$CH_2Cl_2$ (1:1 v/v), respectively. Further single crystal data and the ORTEP projections can be found in Tables S3 and S4 and Fig. S18–S21.

As a reference, the THT crystal structure that was published within our research group showed that the charge transport is governed by columnar stacking of the aromatic core, stabilized by both π-π and π-$CH_3$ interactions along the stacking direction [20]. For **1a**, this cofacially columnar motif is essentially preserved, with molecules arranged in an antiparallel fashion (Fig. 7a). As a consequence, every pair of stacked triindole units is separated by an intercalated AB moiety, resulting in an alternating triindole-triindole-AB columnar architecture. The peripheral triindole aromatic rings are titled 12.1, 3.6 and 0.94° out of plane compared to the central hub, which is less distorted than for THT (10, 14 and 16°). Within each triindole dimer, adjacent molecules are rotated by 30° and exhibit centroid-to-centroid distances of 3.49 Å, which are slightly shorter than those observed for THT (3.63 Å). Despite this tightened π-π stacking, the increased planarity weakens the $CH_3$-π interactions between the *N*-methyl groups and the peripheral centroids from the adjacent molecule (4.06 Å compared to 3.43 Å in THT). Moreover, the columnar stacking is further perturbed by the intercalation of AB units between adjacent triindole dimers, which interrupts direct triindole-triindole contacts along the stacking direction and reduce the continuity of the π-stacking pathway. Within the crystal plane, only weak edge-to-face interactions linked neighboring stacks (4.89 Å), suggesting limited lateral coupling. Nevertheless, these interactions, combined with the short intradimer distances, may enable localized electronic coupling and charge hopping between the stacks. This scenario is consistent with prior theoretical studies on *N*-alkylated triindoles, which identified hopping as the dominant charge-transport mechanism in these systems [17,21]. Such partial connectivity accounted for the moderate hole mobilities observed for **1a** ($\sim 10^{-5}$ $cm^2$ $V^{-1}$ $s^{-1}$ at $6 \times 10^5$ V $cm^{-1}$), indicating that, AB intercalation perturbed the ideal columnar packing without fully abolishing the charge transport within the lattice. On the other side, AB units present a C–N–N–C dihedral angle of 179°, which corresponds to the *trans* configuration, while the two phenyl rings exhibited a notable torsion (41°) due to one of the rings interacting with the adjacent triindole aromatic rings.

Upon incorporation of a second AB unit in **2a**, the molecules adopted

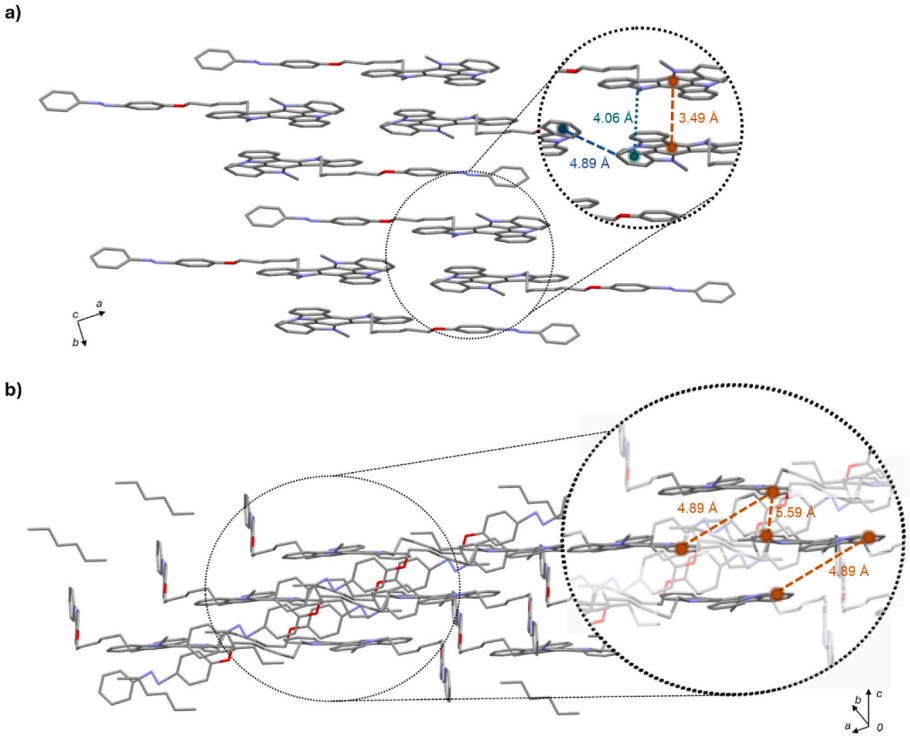


**Fig. 7.** Single crystal structure of a) **1a** and b) **2a**. Key intermolecular interactions are highlighted as: face-to-face π-π (orange), edge-to-face π-π (blue), $CH_3$-π (dark green). The hydrogen atoms were omitted for clarity. (For interpretation of the references to color in this figure legend, the reader is referred to the Web version of this article.)

a slipped columnar packing, where the stacks are aligned in the *a* axis, with sharp discontinuities between stacks due to the placement of the AB subunits in between (Fig. 7b). Although the triiindole cores appear better aligned than in **1a**, the resulting parallel-displaced π-π interactions are long ranged, both along the stacking direction (4.89 Å) and between interdigitated molecules in adjacent columns (5.59 Å). Hence, this arrangement further disrupts effective intermolecular overlap, supporting that additional *N*-bonded AB units in the triindole progressively interferes with charge-transport pathways. Consistent with this structural trend, the $\mu_h$ declined as the AB units increased: **1a** ($1.1 \times 10^{-7}$ $cm^2$ $V^{-1}$ $s^{-1}$), **2a** ($7.2 \times 10^{-8}$ $cm^2$ $V^{-1}$ $s^{-1}$) to **3** (nonoperative), in PC-Z doped films at $6 \times 10^5$ V $cm^{-1}$.

## 4. Conclusions

In summary, this work demonstrates that AB chromophore can be successfully integrated into the triindole backbone while preserving both photoactivity and semiconducting functionality. For this, a novel family of AB-triindole derivatives, by integrating the AB units through a spacer at the nitrogen atoms (*N*-AB-triindoles) or covalently linked at the 3,8,13 positions of the aromatic core (*C*-AB-triindoles) has been successfully designed and synthesized. UV-Vis studies confirmed an efficient and reversible *cis-trans* photoisomerization for all the compounds in solution and in the solid state. More precisely, in *N*-AB-triindoles, the presence of alkyl spacers effectively decoupled the photochromic and semiconducting units, with near-quantitative switching in both directions. In contrast, *C*-AB-triindoles exhibited visible-light-induce *trans*-to-*cis* isomerization due to the extended π-conjugation. In both cases, the materials presented robust photostability over multiple cycles, with thermal back-relaxation half-lives on the hour scale, indicative of bistable photochromic systems. Electrochemical measurements revealed HOMO energy levels in the range of 5.60 to 5.66 eV, which are very similar to those of the triindole itself (5.61 eV for *N*-trihexyltriindole), while a decrease in the solid state in photoemission spectra was observed ($IP_{PE} = 4.99 – 5.13$ eV), supporting air-stable p-type behavior. Hole transport has been further analyzed and confirmed by TOF, with mono-substituted-*N*-AB-triindole derivatives displaying the highest mobilities with up to $1.5 \times 10^{-4}$ $cm^2$ $V^{-1}$ $s^{-1}$ at $6 \times 10^5$ V $cm^{-1}$, while in blends with PC-Z the *C*-AB-triindole derivatives showed a marked enhanced mobilities of $6.4 \times 10^{-5}$ $cm^2$ $V^{-1}$ $s^{-1}$ in the case of the *N*-methylated compound.

## CRediT authorship contribution statement

**Clara Fabregat:** Writing – original draft, Investigation, Data curation. **Jaume Garcia-Amorós:** Writing – review & editing, Funding acquisition. **Dmytro Volyniuk:** Supervision, Resources, Data curation. **Juozas V. Grazulevicius:** Supervision, Resources, Funding acquisition. **Dolores Velasco:** Writing – review & editing, Supervision, Project administration, Funding acquisition, Conceptualization.

## Associated content

The following files are available in the Supporting Information free of charge. Optimization conditions for reaction iii (Table S1), optical properties (Table S2, Fig. S1), $^1$H NMR (Figs. S2 and S3), photoisomerization (Figs. S4 and S5), *cis*-to-*trans* thermal relaxation (Fig. S6–S12), thermal properties (Fig. S13), CV and PES diagrams (Figs. S14 and S15), TOF measurements (Figs. S16 and S17) and single crystal data for derivatives **1a** and **2a** (Tables S3 and S4; Fig. S18–S21).

Single crystal structures for **1a** (CCDC 2538884) and **2a** (CCDC 2539128) can be obtained free of charge from The Cambridge Crystallographic Data Centre via www.ccdc.cam.ac.uk/structures.

## Declaration of competing interest

The authors declare that they have no known competing financial interests or personal relationships that could have appeared to influence the work reported in this paper.

## Acknowledgments

Authors acknowledge the financial support by Ministerio de Ciencia, Innovación y Universidades (grant number PID2023-151915NB-I00) and Horizon Europe, the European Union's framework program for research and innovation (R&I) for 2021-2027, project HELIOS (grant agreement No 101155017). Moreover, C.F is grateful for the predoctoral grant FI AGAUR from Generalitat de Catalunya. The authors want to also thank the CCiTUB for the access to their equipment, with special appreciation to Mercè Font and Cristina Puigjaner (X-Ray Diffraction Unit) for the elucidation of the single-crystal structures.

## Appendix A. Supplementary data

Supplementary data to this article can be found online at https://doi.org/10.1016/j.dyepig.2026.113772.

## Data availability

Data will be made available on request.

## References

[1] Lim D-H, Kang M, Jang S-Y, Hwang K, Kim I-B, Jung E, et al. Unsymmetrical small molecules for broad-band photoresponse and efficient charge transport in organic phototransistors. ACS Appl Mater Interfaces 2020;12:25066–74. https://doi.org/10.1021/acsami.0c02229.

[2] Yang B, Wang Y, Li L, Zhang J, Wang J, Jiao H, et al. High performance ternary organic phototransistors with photoresponse up to 2600 nm at room temperature. Adv Funct Mater 2021;31. https://doi.org/10.1002/adfm.202103787.

[3] Liu Y, Yang Y, Shi D, Xiao M, Jiang L, Tian J, et al. Photo-/Thermal-Responsive field-effect transistor upon blending polymeric semiconductor with hexaarylbiimidazole toward photonically programmable and thermally erasable memory device. Adv Mater 2019;31. https://doi.org/10.1002/adma.201902576.

[4] Tian J, Liu Z, Wu C, Jiang W, Chen L, Shi D, et al. Simultaneous incorporation of two types of azo-groups in the side chains of a conjugated D–A polymer for logic control of the semiconducting performance by light irradiation. Adv Mater 2021;33. https://doi.org/10.1002/adma.202005613.

[5] Carroli M, Dixon AG, Herder M, Pavlica E, Hecht S, Bratina G, et al. Multiresponsive nonvolatile memories based on optically switchable ferroelectric organic field-effect transistors. Adv Mater 2021;33. https://doi.org/10.1002/adma.202007965.

[6] Kumar GS, Neckers DC. Photochemistry of azobenzene-containing polymers. Chem Rev 1989;89:1915–25. https://doi.org/10.1021/cr00098a012.

[7] Rau H. Photoisomerization of azobenzenes. Photoreactive organic thin films. Elsevier; 2002. p. 3–47. https://doi.org/10.1016/B978-012635490-4/50002-0.

[8] Bandara HMD, Burdette SC. Photoisomerization in different classes of azobenzene. Chem Soc Rev 2012;41:1809–25. https://doi.org/10.1039/C1CS15179G.

[9] Hartley GS. The *cis*-form of azobenzene and the velocity of the thermal *cis→trans*-conversion of azobenzene and some derivatives. J Chem Soc 1938;0:633–42. https://doi.org/10.1039/JR9380000633.

[10] Knie C, Utecht M, Zhao F, Kulla H, Kovalenko S, Brouwer AM, et al. *Ortho*-fluoroazobenzenes: visible light switches with very long-lived *Z* isomers. Chem Eur J 2014;20:16492–501. https://doi.org/10.1002/chem.201404649.

[11] Garcia-Amorós J, Reig M, Cuadrado A, Ortega M, Nonell S, Velasco D. A photoswitchable bis-azo derivative with a high temporal resolution. Chem Commun 2014;50:11462–4. https://doi.org/10.1039/C4CC05331A.

[12] Garcia-Amorós J, Martínez M, Finkelmann H, Velasco D. Kinetico-mechanistic study of the thermal *cis-to-trans* isomerization of 4,4′-Dialkoxyazoderivatives in nematic liquid crystals. J Phys Chem B 2010;114:1287–93. https://doi.org/10.1021/jp909557h.

[13] García-Amorós J, Velasco D. Recent advances towards azobenzene-based light-driven real-time information-transmitting materials. Beilstein J Org Chem 2012;8:1003–17. https://doi.org/10.3762/bjoc.8.113.

[14] Arlt M, Scheffler A, Suske I, Eschner M, Saragi TPI, Salbeck J, et al. Bipolar redox behaviour, field-effect mobility and transistor switching of the low-molecular azo glass AZOPD. Phys Chem Chem Phys 2010;12:13828. https://doi.org/10.1039/c0cp00643b.

[15] Chen Y, Li C, Xu X, Liu M, He Y, Murtaza I, et al. Thermal and optical modulation of the carrier mobility in OTFTs based on an azo-anthracene liquid crystal organic

semiconductor. ACS Appl Mater Interfaces 2017;9:7305–14. https://doi.org/10.1021/acsami.6b13500.
[16] Li M, Zheng J, Wang X, Yu R, Wang Y, Qiu Y, et al. Light-responsive self-strained organic semiconductor for large flexible OFET sensing array. Nat Commun 2022;13:4912. https://doi.org/10.1038/s41467-022-32647-9.
[17] Reig M, Bagdziunas G, Ramanavicius A, Puigdollers J, Velasco D. Interface engineering and solid-state organization for triindole-based p-type organic thin-film transistors. Phys Chem Chem Phys 2018;20:17889–98. https://doi.org/10.1039/C8CP02963F.
[18] Cuadrado A, Bujaldón R, Fabregat C, Puigdollers J, Velasco D. Confronting positions: *Para*- vs. *meta*-functionalization in triindole for p-type air-stable OTFTs. Org Electron 2024;128:107020. https://doi.org/10.1016/j.orgel.2024.107020.
[19] Iino H, Usui T, Hanna J. Liquid crystals for organic thin-film transistors. Nat Commun 2015;6:6828. https://doi.org/10.1038/ncomms7828.
[20] Reig M, Puigdollers J, Velasco D. Molecular order of air-stable p-type organic thin-film transistors by tuning the extension of the π-conjugated core: the cases of indolo[3,2-*b*]carbazole and triindole semiconductors. J Mater Chem C Mater 2015;3:506–13. https://doi.org/10.1039/C4TC01692K.
[21] Ruiz C, Arrechea-Marcos I, Benito-Hernández A, Gutierrez-Puebla E, Monge MA, López Navarrete JT, et al. Solution-processed *N*-trialkylated triindoles for organic field effect transistors. J Mater Chem C Mater 2018;6:50–6. https://doi.org/10.1039/C7TC03866F.
[22] Averdunk C, Shamsabadi M, Moth-Poulsen K, Wegner HA. Structure–property relationship of *p*-alkoxyazobenzenes as molecular solar thermal phase change material energy storage systems (MOST-PCM). J Mater Chem C Mater 2025;13:13337–46. https://doi.org/10.1039/D5TC01024A.
[23] Maddala S, Panua A, Venkatakrishnan P. Steering scholl oxidative heterocoupling by tuning topology and electronics for building thiananographenes and their functional N−/C−Congeners. Chem Eur J 2021;27:16013–20. https://doi.org/10.1002/chem.202102920.
[24] Loan T, Santra M, Bradley M. Novel class of photochromic molecules exhibiting photo-switching in the solid state. Front Chem 2023;11. https://doi.org/10.3389/fchem.2023.1205452.
[25] Zhao C, Wang T, Li D, Lu T, Liu D, Meng Q, et al. Synthesis and characterization of triphenylamine modified azobenzene dyes. Dyes Pigments 2017;137:256–64. https://doi.org/10.1016/j.dyepig.2016.10.018.
[26] Anggia IS, Hayati D, Hong J. Synthesis and photophysical characterization of push-pull azobenzene derivatives featuring different π-bridges for photoresponsive applications. Dyes Pigments 2025;234:112550. https://doi.org/10.1016/j.dyepig.2024.112550.
[27] Konrad DB, Savasci G, Allmendinger L, Trauner D, Ochsenfeld C, Ali AM. Computational design and synthesis of a deeply red-shifted and bistable azobenzene. J Am Chem Soc 2020;142:6538–47. https://doi.org/10.1021/jacs.9b10430.
[28] Lameijer LN, Budzak S, Simeth NA, Hansen MJ, Feringa BL, Jacquemin D, et al. General principles for the design of visible-light-responsive photoswitches: tetra-*ortho*-chloro-azobenzenes. Angew Chem Int Ed 2020;59:21663–70. https://doi.org/10.1002/anie.202008700.
[29] Isokuortti J, Kuntze K, Virkki M, Ahmed Z, Vuorimaa-Laukkanen E, Filatov MA, et al. Expanding excitation wavelengths for azobenzene photoswitching into the near-infrared range via endothermic triplet energy transfer. Chem Sci 2021;12:7504–9. https://doi.org/10.1039/d1sc01717a.
[30] Bléger D, Hecht S. Visible-light-activated molecular switches. Angew Chem Int Ed 2015;54:11338–49. https://doi.org/10.1002/anie.201500628.
[31] Bujak K, Wasiak A, Sobolewska A, Bartkiewicz S, Malecki JG, Nycz JE, et al. A family of azoquinoline derivatives: effect of the substituent at azo linkage on thermal *cis-trans* isomerization based on an experimental and computational approach. Dyes Pigments 2020;175:108151. https://doi.org/10.1016/j.dyepig.2019.108151.
[32] Porcu P, Estrada-Montaño AS, Vonlanthen M, Cuétara-Guadarrama F, González-Méndez I, Sorroza-Martínez K, et al. Azobenzene dyads containing fullerene, porphyrin and pyrene chromophores: molecular design and optical properties. Dyes Pigments 2022;197:109858. https://doi.org/10.1016/j.dyepig.2021.109858.
[33] Chi H, Mya KY, Lin T, He C, Wang F, Chin WS. Thermally stable azobenzene dyes through hybridization with POSS. New J Chem 2013;37:735. https://doi.org/10.1039/c2nj40977a.
[34] Ling MM, Bao Z. Thin film deposition, patterning, and printing in organic thin film transistors. Chem Mater 2004;16:4824–40. https://doi.org/10.1021/cm0496117.
[35] Seifrid M, Ford MJ, Li M, Koh KM, Trefonas P, Bazan GC. Electrical performance of a molecular organic semiconductor under thermal stress. Adv Mater 2017;29. https://doi.org/10.1002/adma.201605511.
[36] Griffiths JII. Photochemistry of azobenzene and its derivatives. Chem Soc Rev 1972;1:481. https://doi.org/10.1039/cs9720100481.
[37] Takimiya K, Yamamoto T, Ebata H, Izawa T. Design strategy for air-stable organic semiconductors applicable to high-performance field-effect transistors. Sci Technol Adv Mater 2007;8:273–6. https://doi.org/10.1016/j.stam.2007.02.010.
[38] Tang CG, Hou K, Leong WL. The quest for air stability in organic semiconductors. Chem Mater 2024;36:28–53. https://doi.org/10.1021/acs.chemmater.3c02093.
[39] Dost R, Das A, Grell M. Time-of-flight mobility measurements in organic field-effect transistors. J Appl Phys 2008;104. https://doi.org/10.1063/1.3006443.
[40] Vajiravelu S, Ramunas L, Juozas Vidas G, Valentas G, Vygintas J, Valiyaveettil S. Effect of substituents on the electron transport properties of bay substituted perylene diimide derivatives. J Mater Chem 2009;19:4268. https://doi.org/10.1039/b901847f.
[41] Reghu RR, Bisoyi HK, Grazulevicius JV, Anjukandi P, Gaidelis V, Jankauskas V. Air stable electron-transporting and ambipolar bay substituted perylene bisimides. J Mater Chem 2011;21:7811. https://doi.org/10.1039/c1jm11091h.
[42] Andrikaityte E, Simokaitiene J, Tomkeviciene A, Grazulevicius JV, Jankauskas V. Synthesis and properties of triindole-based monomers and polymers. Molecular crystals and liquid. Crystals 2014;590:121–9. https://doi.org/10.1080/15421406.2013.873856.